

# Estimating Spatially-Smoothed Fiber Orientation Distribution from Diffusion-MRI Experiments

Jilei Yang \*

Department of Statistics, University of California, Davis

Seungyong Hwang\*

Department of Genetics, Stanford University

and

Jie Peng<sup>†</sup>

Department of Statistics, University of California, Davis

## Abstract

Diffusion-weighted magnetic resonance imaging (D-MRI) is an in-vivo and non-invasive imaging technology to probe anatomical architectures of biological samples. One of the most important applications of D-MRI is to reconstruct the white matter fiber tracts in the brain, which reveals the connectivity patterns among different brain regions and helps us to understand how brain works. In this paper, we propose a novel *Nearest-neighbor Adaptive Regression Model (NARM)* for adaptive estimation of the fiber orientation distribution (FOD) function based on D-MRI data through leveraging spatial homogeneity of fiber orientations and incorporating neighborhood information. We formulate the FOD estimation problem as a weighted linear regression problem, where the weights account for spatial proximity and potential heterogeneity due to different fiber configurations. Moreover, a stopping rule based on nearest neighbor distance is designed to prevent over-smoothing. Comprehensive simulation results demonstrate that NARM improves voxel-wise estimation and performs better than a competing spatial smoothing method. We apply NARM to the *Human Connectome Project (HCP)* test-retest data, and show that fiber tracts reconstruction based on the NARM FOD estimation is generally more consistent between the test and re-test D-MRI data of the same subject than that based on the voxel-wise FOD estimation. This attests to the practical value of NARM for analyzing D-MRI data.

*Keywords:* propagation-separation method, minimum nearest-neighbor distance, HCP

---

\*Co-first authors

<sup>†</sup>Correspondence author: jiepeng@ucdavis.edu

# 1 Introduction

The study of the brain anatomical structure and how it relates to brain functions is an old yet essential topic. As an in-vivo, non-invasive and non-radioactive medical imaging technology, diffusion-weighted magnetic resonance imaging (D-MRI) has become widely used to probe architecture of the brain. The detailed anatomy of white matter fiber tracts in the brain can be revealed by making use of diffusion displacement measures of water molecules through D-MRI, as water diffuses faster along the fiber bundles and D-MRI signal is sensitized with water movements (both direction and rate). Reconstructing white matter fiber tracts is of great value in understanding the brain structural connectivity and its functionality (Mori 2007, Sporns 2010). One of the earliest D-MRI technology is the well-known *diffusion tensor imaging (DTI)* (Basser et al. 1994) where a tensor is used to summarize water diffusion at each brain voxel. More recently, *high angular resolution diffusion imaging (HARDI)* has become popular due to its ability in accurate extraction of orientation information of intra-voxel crossing fibers (Tuch et al. 2002). Once the voxel-wise water diffusion/fiber orientation information is extracted, the white matter fiber tracts are then reconstructed by applying tracking algorithms, a process called tractography (Basser et al. 2000, Wong et al. 2016).

Several models have been proposed for the HARDI data, including angular reconstruction models such as *fiber orientation distribution (FOD)* (Tournier et al. 2004, 2007) and *diffusion orientation distribution function (ODF)* (Tuch 2004, Descoteaux et al. 2007, 2009). In this paper, we focus on the FOD model, which is designed to describe the angular dependence of the axonal fiber bundles by making use of sharp geometric features of the FOD (Jensen et al. 2016).

The FOD model is based on the spherical deconvolution framework described in Tournier et al. (2004, 2007). The key to an accurate FOD estimation is a parsimonious representation of the FOD in a suitable basis since deconvolution is an inverse problem and is susceptible to noise amplification. Early studies of FOD estimation are mostly based on the spherical harmonics (SH) representations since FODs are spherical probability density functions (Tournier et al. 2004, 2007). However, due to the global support of the SH basis functions, they do not provide an efficient presentation of FOD where spiky features (i.e.,

peaks) are present when there are a small number of well-defined fiber bundles in a voxel. Recently, Yan et al. (2018) proposed an FOD estimation method called **SN-lasso** based on the spherical needlets (SN) representation. As smooth spherical functions localized in both space and frequency, spherical needlets form a tight frame and provide parsimonious and stable representations for spherical functions with localized sharp peaks (Narcowich et al. 2006*b,a*). Through the spherical needlets representation, the FOD estimation problem is reformulated as a linear regression problem where the needlet coefficients of the FOD are the regression coefficients. An  $l_1$  penalty is imposed on the needlet coefficients to ensure a sparse representation. Moreover, a nonnegative constraint is imposed on the estimated FOD. In this paper, we focus on the **SN-lasso** method in FOD estimation, as it is shown to lead to more accurate estimation of the FOD and preserve the sharp features (peaks) of FOD that are used as inputs for subsequent tractography Yan et al. (2018).

Most existing methods for water diffusion/fiber orientation estimation, including **SN-lasso**, are developed to perform voxel-wise estimation separately, where the spatial constraint of the fibers is essentially ignored. However, the orientation of a single fiber bundle is expected to vary smoothly (at least for the most part) from one voxel to the next, until it reaches the boundary. Such spatial homogeneity means that it is possible to aggregate data from neighboring voxels to obtain a more precise estimation at each voxel.

A few methods have been proposed for D-MRI data where spatial constraint is incorporated. Some of these methods are based on the well-known *propagation-separation* method (Polzehl & Spokoiny 2000, 2006), which is developed for estimating functions with large homogeneous regions and sharp discontinuities. Although the original propagation-separation method is only applicable in denoising images, several extensions are made for modeling D-MRI data, e.g., smoothing and estimation of DTI data via an anisotropic structural adaptive smoothing procedure (Tabelow et al. 2008), smoothing raw HARDI images based on structural adaptive smoothing in both voxel space and diffusion-gradient space (Becker et al. 2012, 2014), spatial and adaptive analysis of neuroimaging data using a multiscale adaptive regression model (**MARM**) which integrates propagation-separation method with voxel-wise statistical modeling (Li et al. 2011), spatial and adaptive estimation of ODF using a penalized multiscale adaptive regression model (**PMARM**) which integrates

MARM, propagation-separation method and Lasso (Rao et al. 2016). Other spatial smoothing methods include spatial smoothing and estimation of DTI (Liu et al. 2013, Yu & Li 2013), spatial smoothing of HARDI with Bayesian spatial regularization (Raj et al. 2011), spatial smoothing of estimated diffusion directions via clustering (Wong et al. 2016).

In this paper, we propose a novel *Nearest-neighbor Adaptive Regression Model* (NARM) to conduct spatially smoothed and locally adaptive estimation of FODs across all voxels. NARM can be regarded as an integration of the propagation-separation approach and the voxel-wise FOD estimation via SN-lasso. Specifically, for the FOD estimation at each voxel, instead of optimizing a single likelihood function based on data from this voxel itself, we incorporate its neighborhood information by optimizing the sum of weighted likelihood functions based on data from this voxel as well as its neighboring voxels. The weights are chosen to account for both spatial proximity and potential heterogeneity due to the presence of crossing fibers, and are calculated based on both the spatial distance between a neighboring voxel and the target voxel and the similarity between their respective FOD estimates in the previous step.

Similar to the PMARM method in Rao et al. (2016), we adaptively update these weights and use a stopping rule to avoid over-smoothing. However, NARM differs from PMARM in three major aspects. First, we use Hellinger distance to measure similarity between FOD estimates. Hellinger distance is proposed specifically for probability density functions and is more sensitive to FOD peak differences. In contrast, the PMARM method uses the Euclidean distance. Second, we use a simple yet effective stopping rule based on the minimum distance between the target voxel and its nearest neighbor(s), whereas the PMARM method relies on a more complicated stopping rule with hyper-parameters that are hard to tune in practice. Third, we implement a novel weight-rescaling scheme to mitigate over-smoothing/under-smoothing issues.

We conduct extensive simulation experiments on two-dimensional and three-dimensional regions to demonstrate the effectiveness of the NARM method, and its superior performance over the voxel-wise SN-lasso method and the PMARM method (adapted for FOD estimation). Moreover, we apply NARM to the test-retest D-MRI data set of 35 subjects from the WU-Minn Human Connectome Project (HCP) (Van Essen et al. 2013). We focus on a region

where two major white-matter fiber tracts, namely, the superior longitudinal fasciculus (SLF) and the corticospinal tract (CST), are crossing. For each subject, we reconstruct these two tracts (confined in this region) twice: once using the test D-MRI data and another time using the re-test D-MRI data. We find that the “test and re-test” tractography results derived from the **NARM** method estimated FODs tend to be more consistent compared to those based on the voxel-wise **SN-lasso** estimates.

The rest of paper is organized as follows. Section 2 formally introduces the FOD model and describes the voxel-wise FOD estimation method **SN-lasso**. Section 3 proposes the *Nearest-neighbor Adaptive Regression Model* (**NARM**) for FOD estimation. Section 4 and 5 present the experimental results on synthetic and real D-MRI data, respectively. Section 6 concludes our work and discusses future directions. Additional details are deferred to a Supplementary Material.

## 2 Voxel-wise FOD estimation

In this section, we first introduce the FOD model for D-MRI data (Tournier et al. 2004) and then describe the voxel-wise **SN-lasso** FOD estimation based on the spherical needelts representation and  $\ell_1$  penalized regression (Yan et al. 2018).

### 2.1 Fiber orientation distribution

D-MRI data consist of diffusion weighted signal measurements on a 3D spatial grid (of the sample) along a set of predetermined gradient directions. For example, D-MRI data from HCP have diffusion weighted measurements along a set of 90 distinct gradient directions (for each b-value) at each voxel on a  $145 \times 174 \times 145$  3D brain grid.

Under the fiber orientation distribution (FOD) model for D-MRI (Tournier et al. 2004, 2007), the diffusion signal function  $S(\mathbf{v}, \cdot)$  at voxel  $\mathbf{v}$  is modeled as a spherical convolution of an FOD function  $F(\mathbf{v}, \cdot): \mathbb{S}^2 \rightarrow \mathbb{R}^+$ , a symmetric spherical probability density function describing the population of fiber bundle orientations at  $\mathbf{v}$ , and a response function  $R(\cdot): L^1([-1, 1]) \rightarrow \mathbb{R}$ , an azimuthal symmetric kernel function representing the water diffusion

characteristics along a single fiber bundle aligned with the  $z$ -axis:

$$S(\mathbf{v}, \mathbf{x}) = R * F(\mathbf{v}, \mathbf{x}) = \int_{\mathbb{S}^2} R(\mathbf{x}^T \mathbf{y}) F(\mathbf{v}, \mathbf{y}) d\omega(\mathbf{y}), \quad \mathbf{x} \in \mathbb{S}^2. \quad (1)$$

Note that the FOD  $F(\mathbf{v}, \cdot)$  is voxel-dependent and the response function  $R(\cdot)$  is assumed to be the same across all voxels.

The observed diffusion measurements at voxel  $\mathbf{v}$ ,  $\mathbf{y}(\mathbf{v}) = \{y_i(\mathbf{v})\}_{i=1}^n$ , are regarded as the noise corrupted evaluations of the diffusion signal function  $S(\mathbf{v}, \cdot)$  at  $n$  gradient directions  $\{\mathbf{x}_i \in \mathbb{S}^2\}_{i=1}^n$ . The goal is to estimate the FOD function  $F(\mathbf{v}, \cdot)$  at each voxel based on the observed diffusion measurements. In practice, the response function  $R(\cdot)$  is pre-estimated and specified, e.g., through applying the single tensor model (Basser et al. 1994) to voxels with a clear single dominant fiber bundle (see Yan et al. (2018) for details). Hereafter  $R(\cdot)$  is treated as given.

## 2.2 SN-lasso

Following Descoteaux et al. (2007), Yan et al. (2018), the real symmetric spherical harmonic (SH) functions  $\{\Phi_{lm} : m = -l, \dots, l\}_{l=0,2,4,\dots}$  form an orthonormal basis for the square integrable real symmetric functions on  $\mathbb{S}^2$ . By the orthonormality of the SH basis, the diffusion signal function  $S(\mathbf{v}, \mathbf{x})$  can be expressed as:

$$S(\mathbf{v}, \mathbf{x}) = \sum_l \sum_{m=-l}^l s_{lm} \Phi_{lm}(\mathbf{x}) = \sum_l \sqrt{\frac{4\pi}{2l+1}} r_l \sum_{m=-l}^l f_{lm} \Phi_{lm}(\mathbf{x}),$$

where  $s_{lm} := \langle S, \Phi_{lm} \rangle$ ,  $r_l := \langle R, \Phi_{l0} \rangle$  and  $f_{lm} := \langle F, \Phi_{lm} \rangle$  are the spherical harmonic coefficients of the diffusion signal function, response function  $R(\cdot)$  and FOD  $F(\mathbf{v}, \cdot)$ , respectively.

Assume the SH basis up to level  $l_{\max}$  can provide good approximations for the diffusion signal function, the response function and the FOD. Then, the observed diffusion weighted measurements  $\mathbf{y}(\mathbf{v})$  can be modeled as:

$$\mathbf{y}(\mathbf{v}) = \mathbf{\Phi} \mathbf{R} \mathbf{f}(\mathbf{v}) + \boldsymbol{\epsilon}, \quad (2)$$

where  $\mathbf{\Phi}$  is an  $n \times L$  matrix (with  $L = (l_{\max} + 1)(l_{\max} + 2)/2$  being the number of SH basis functions) consisting of SH basis functions' evaluations at the  $n$  gradient directions;  $\mathbf{R}$  is

an  $L \times L$  diagonal matrix with  $\sqrt{\frac{4\pi}{2l+1}}r_l\mathbf{I}_{2l+1}$  for the  $l$ th diagonal block;  $\mathbf{f}(\mathbf{v})$  is an  $L \times 1$  vector of the FOD  $F(\mathbf{v}, \cdot)$ 's SH coefficients; and  $\boldsymbol{\epsilon}$  is an  $n \times 1$  error vector.

Since FODs are either constant (when there is no distinct fiber bundle at the voxel) or with a few localized sharp peaks (where each peak corresponds to a major fiber bundle direction at the voxel), SH functions are not efficient basis for representing FODs due to their global support. In **SN-lasso**, FODs are instead represented by symmetric spherical needlets (SN) basis (Narcowich et al. 2006a). The SN functions are constructed using SH functions and they form a tight frame for the square integrable real symmetric functions on  $\mathbb{S}^2$ . Moreover, they are localized in both scale and space and thus FODs can be well approximated by a small set of SN functions.

We set the maximum level of SN basis  $j_{\max} = \lceil \log_2(l_{\max}) \rceil$  and  $N = 2^{2j_{\max}+3} - 1$  being the corresponding number of SN basis functions. The order  $j_{\max}$  is set such that the first  $N$  SN basis functions can linearly represent the SH basis functions up to level  $l_{\max}$ . In this case, the SH coefficient vector  $\mathbf{f}(\mathbf{v})$  in (2) can be expressed as  $\mathbf{C}\boldsymbol{\beta}(\mathbf{v})$ , where  $\mathbf{C}$  is an  $L \times N$  transition matrix and can be pre-computed, and  $\boldsymbol{\beta}(\mathbf{v})$  is an  $N \times 1$  vector of the FOD  $F(\mathbf{v}, \cdot)$ 's SN coefficients (Yan et al. 2018). Consequently, Eq. (2) can then be rewritten accordingly as:

$$\mathbf{y}(\mathbf{v}) = \boldsymbol{\Phi}\mathbf{R}\mathbf{C}\boldsymbol{\beta}(\mathbf{v}) + \boldsymbol{\epsilon}. \quad (3)$$

Based on the sparsity nature of the SN coefficients  $\boldsymbol{\beta}(\mathbf{v})$ , **SN-lasso** estimates  $\boldsymbol{\beta}(\mathbf{v})$  by an  $l_1$ -penalized linear regression model subject to a nonnegativity constraint:

$$\hat{\boldsymbol{\beta}}(\mathbf{v}) = \arg \min_{\boldsymbol{\beta}(\mathbf{v}): \tilde{\boldsymbol{\Phi}}\mathbf{C}\boldsymbol{\beta}(\mathbf{v}) \succeq \mathbf{0}} \frac{1}{2} \|\mathbf{y}(\mathbf{v}) - \boldsymbol{\Phi}\mathbf{R}\mathbf{C}\boldsymbol{\beta}(\mathbf{v})\|_2^2 + \lambda \|\boldsymbol{\beta}(\mathbf{v})\|_1. \quad (4)$$

Here  $\lambda \|\boldsymbol{\beta}(\mathbf{v})\|_1$  is the lasso regularizer with tuning parameter  $\lambda \geq 0$ , which leads to a sparse estimate of  $\boldsymbol{\beta}(\mathbf{v})$ ;  $\tilde{\boldsymbol{\Phi}}$  is the matrix of the  $L$  SH basis functions evaluated on a dense spherical grid, and  $\tilde{\boldsymbol{\Phi}}\mathbf{C}\boldsymbol{\beta}(\mathbf{v}) \succeq \mathbf{0}$  (element-wise non-negative) guarantees that the estimated FOD on this dense grid is nonnegative. Notice both the design matrix  $\boldsymbol{\Phi}\mathbf{R}\mathbf{C}$  and the constraint matrix  $\tilde{\boldsymbol{\Phi}}\mathbf{C}$  are the same across all voxels and can be computed in advance.

A computationally efficient algorithm based on ADMM (*Alternating Directions Method of Multipliers*) (Boyd et al. 2011) was developed for the optimization problem in (4). A peak detection algorithm is also proposed to efficiently identify major fiber directions

according to an estimated FOD, and these peak directions are subsequently used as inputs for tractography algorithms for fiber tracts reconstruction. More details can be found in Yan et al. (2018).

### 3 Spatially-smoothed FOD estimation

The **SN-lasso** method described in the previous section is a voxel-wise method which estimates the FOD at each voxel independently by using only the D-MRI measurements from that voxel itself. The spatial information contained in the D-MRI measurements is essentially ignored by this method.

For each fiber bundle (if any) at a voxel, it is expected to smoothly continue into a neighboring voxel along its fiber direction, except at the boundaries between fiber tracts. See Figure 1(a) for an illustration on a two-dimensional region. This spatial constraint is very important and can be utilized to improve FOD estimation and the subsequent reconstruction of fiber tracts. Here, we propose a spatial smoothing method in FOD estimation, named *Nearest-neighbor Adaptive Regression Model* (**NARM**). The underlying idea of **NARM** is the local likelihood modeling (Fan & Gijbels 1996), that is, instead of optimizing a single log-likelihood function at voxel  $\mathbf{v}$  based on the observed diffusion measurements  $\mathbf{y}(\mathbf{v})$  from voxel  $\mathbf{v}$ , we incorporate measurements from its neighboring voxels as well and optimize the sum of the weighted log-likelihood functions within a neighborhood centered at voxel  $\mathbf{v}$ .

Let  $N_d(\mathbf{v}) := \{\mathbf{v}' : \|\mathbf{v} - \mathbf{v}'\|_2 \leq d\}$  denote a (spherical) neighborhood with radius  $d$  centered at voxel  $\mathbf{v}$ , and  $\omega_d(\mathbf{v}, \mathbf{v}')$  denote a weight function of pair  $(\mathbf{v}, \mathbf{v}')$  such that  $\sum_{\mathbf{v}' \in N_d(\mathbf{v})} \omega_d(\mathbf{v}, \mathbf{v}') = 1$  and  $\omega_d(\mathbf{v}, \mathbf{v}') \geq 0$ . Then  $\hat{\boldsymbol{\beta}}_d(\mathbf{v})$  denotes the SN coefficients estimates by an  $l_1$ -penalized weighted linear regression model:

$$\begin{aligned} \hat{\boldsymbol{\beta}}_d(\mathbf{v}) &:= \arg \min_{\boldsymbol{\beta}(\mathbf{v}): \boldsymbol{\Phi} \mathbf{R} \mathbf{C} \boldsymbol{\beta}(\mathbf{v}) \succ \mathbf{0}} \sum_{\mathbf{v}' \in N_d(\mathbf{v})} \omega_d(\mathbf{v}, \mathbf{v}') \cdot \frac{1}{2} \|\mathbf{y}(\mathbf{v}') - \boldsymbol{\Phi} \mathbf{R} \mathbf{C} \boldsymbol{\beta}(\mathbf{v})\|_2^2 + \lambda \|\boldsymbol{\beta}(\mathbf{v})\|_1 \\ &= \arg \min_{\boldsymbol{\beta}(\mathbf{v}): \boldsymbol{\Phi} \mathbf{R} \mathbf{C} \boldsymbol{\beta}(\mathbf{v}) \succ \mathbf{0}} \frac{1}{2} \|\mathbf{y}_d(\mathbf{v}) - \boldsymbol{\Phi} \mathbf{R} \mathbf{C} \boldsymbol{\beta}(\mathbf{v})\|_2^2 + \lambda \|\boldsymbol{\beta}(\mathbf{v})\|_1, \end{aligned} \tag{5}$$

where  $\mathbf{y}_d(\mathbf{v}) = \sum_{\mathbf{v}' \in N_d(\mathbf{v})} \omega_d(\mathbf{v}, \mathbf{v}') \mathbf{y}(\mathbf{v}')$  is the weighted average of observed diffusion measurements within the neighborhood  $N_d(\mathbf{v})$ . Note that when  $d$  is set to be 0, the neighbor-



hood  $N_d(\mathbf{v})$  contains only the voxel  $\mathbf{v}$ , and Eq. (5) coincides with Eq. (4) in the voxel-wise method **SN-lasso**. Following Yan et al. (2018), in practice, we select the largest value of the tuning parameter  $\lambda$  for the  $l_1$  penalty such that the residual sum of squares can not be significantly improved when the value of  $\lambda$  is further decreased.

One popular approach in local likelihood modeling is the *propagation-separation* method (Polzehl & Spokoiny 2000, 2006), which aims to find a maximal local neighborhood for each sample point where the local homogeneity assumption of the parameters holds. Inspired by the propagation-separation method, we adaptively determine the weight  $\omega_d(\mathbf{v}, \mathbf{v}')$  as follows: At voxel  $\mathbf{v}$ , we construct a sequence of nested (spherical) neighborhoods with increasing radii  $0 = d_0 < d_1 < \dots < d_S$ . At  $d_0 = 0$ , the estimated coefficients  $\hat{\beta}_{d_0}(\mathbf{v})$  are exactly  $\hat{\beta}(\mathbf{v})$  – the **SN-lasso** estimates by Eq. (4); At the  $s$ th step, the weights  $\omega_{d_s}(\mathbf{v}, \mathbf{v}')$  are calculated as detailed in the following subsections where the information of the previously estimated coefficients  $\hat{\beta}_{d_{s-1}}(\mathbf{v})$  is utilized.

In practice, we set the sequence of  $d_s$  as  $d_0 = 0$ ,  $d_s = r^s$ ,  $s = 1, \dots, S$ , where the default choice of  $r$  is  $r = 1.15$  and the default choice of  $S$  is  $S = 10$  for two-dimensional regions and  $S = 6$  for three-dimensional regions. The intuition of different choices of  $S$  is so that the number of voxels in the largest neighborhood  $N_{d_S}(\mathbf{v})$  in a two-dimensional region and that in a three-dimensional region are comparable.

### 3.1 Weight function

The weights  $\omega_d(\mathbf{v}, \mathbf{v}')$ ,  $\mathbf{v}' \in N_d(\mathbf{v})$  are crucial for the success of **NARM**. First, the weights should reflect spatial proximity: the closer a voxel is to  $\mathbf{v}$ , the more information is contained in its D-MRI measurements about the FOD at  $\mathbf{v}$ . Second, the weights should also reflect similarity between the underlying fiber configurations. That is, the weight  $\omega_d(\mathbf{v}, \mathbf{v}')$  should be large if the fiber configurations at the two voxels  $\mathbf{v}$  and  $\mathbf{v}'$  are similar; On the other hand, if the fiber configurations at the two voxels are very different, the weight should be small to prevent incorporating signals from different fiber tracts. For example, in Figure 1(a), the voxel on the third row and the second column has very different fiber configurations from the voxel on the third row and the third column: the former voxel has only one fiber bundle, whereas the latter has two crossing fiber bundles. Therefore, the weight for this pair should

be small despite they are next to each other. As the underlying fiber configurations are unknown a priori, a natural idea is to use the estimated FODs from the previous step to help calculate the weights in the current step.

Specifically, the proposed weights at step  $s$  is:

$$\omega_{d_s}(\mathbf{v}, \mathbf{v}') := \frac{K_{\text{loc}}(\|\mathbf{v} - \mathbf{v}'\|_2/d_s)K_{\text{sim}}(\gamma \cdot \text{Dist}_s(\mathbf{v}, \mathbf{v}'))}{\sum_{\mathbf{v}' \in N_{d_s}(\mathbf{v})} K_{\text{loc}}(\|\mathbf{v} - \mathbf{v}'\|_2/d_s)K_{\text{sim}}(\gamma \cdot \text{Dist}_s(\mathbf{v}, \mathbf{v}'))} \quad (6)$$

where  $\text{Dist}_s(\mathbf{v}, \mathbf{v}')$  is a similarity measure between the estimated FODs at voxels  $\mathbf{v}$  and  $\mathbf{v}'$ ,  $K_{\text{loc}}(\cdot)$ ,  $K_{\text{sim}}(\cdot)$  are two nonnegative kernel functions and  $\gamma > 0$  is a smoothness parameter. The weight  $\omega_{d_s}(\mathbf{v}, \mathbf{v}')$  in Eq. (6) has two parts: the spatial weight  $\omega_{\text{loc}, d_s}(\mathbf{v}, \mathbf{v}') := K_{\text{loc}}(\|\mathbf{v} - \mathbf{v}'\|_2/d_s)$  and the similarity weight  $\omega_{\text{sim}, d_s}(\mathbf{v}, \mathbf{v}') := K_{\text{sim}}(\gamma \cdot \text{Dist}_s(\mathbf{v}, \mathbf{v}'))$ . We choose  $K_{\text{loc}}(u) = (1 - u^2)_+$  which assigns a positive weight only to the voxels within the neighborhood  $N_{d_s}(\mathbf{v})$ . Moreover, it gives more weight to voxels spatially closer to the target voxel  $\mathbf{v}$ . We choose  $K_{\text{sim}}(u) = \exp(-u^2)$  which takes a small value if the estimated FODs at voxels  $\mathbf{v}'$  and  $\mathbf{v}$  differ significantly, i.e, when the dissimilarity measure  $\text{Dist}_s(\mathbf{v}, \mathbf{v}')$  is large.

Moreover, the smoothness parameter  $\gamma > 0$  controls how fast the weight decreases with the increase of the dissimilarity measure: a large  $\gamma$  means faster decrease of the weight with dissimilarity between FODs at the two voxels and thus less aggressive smoothing. In practice, we set  $\gamma = 2$  at  $b = 1000s/mm^2$  and  $\gamma = 4$  at  $b = 3000s/mm^2$ . The intuition is that we should slow down slightly the smoothing process as  $b$ -value increases, since larger  $b$ -value means stronger diffusion signals and more reliable voxel-wise FOD estimation (and thus less benefit from smoothing).

As for the dissimilarity measure  $\text{Dist}_s(\mathbf{v}, \mathbf{v}')$ , we propose to use the *Hellinger distance* between the previously estimated FOD (represented on a dense grid specified by  $\tilde{\Phi}$ ) at voxel  $\mathbf{v}$ ,  $\hat{\mathbf{f}}_{d_{s-1}}(\mathbf{v}) := \tilde{\Phi}\mathbf{C}\hat{\beta}_{d_{s-1}}(\mathbf{v})/\|\tilde{\Phi}\mathbf{C}\hat{\beta}_{d_{s-1}}(\mathbf{v})\|_2$ , and the previously estimated FOD at voxel  $\mathbf{v}'$ ,  $\hat{\mathbf{f}}_{d_{s-1}}(\mathbf{v}') := \tilde{\Phi}\mathbf{C}\hat{\beta}_{d_{s-1}}(\mathbf{v}')/\|\tilde{\Phi}\mathbf{C}\hat{\beta}_{d_{s-1}}(\mathbf{v}')\|_2$ . Specifically,  $\text{Dist}_s(\mathbf{v}, \mathbf{v}')$  is given by:

$$\text{Dist}_s(\mathbf{v}, \mathbf{v}') := \frac{1}{\sqrt{2}} \left\| \left\| \sqrt{\hat{\mathbf{f}}_{d_{s-1}}(\mathbf{v})} - \sqrt{\hat{\mathbf{f}}_{d_{s-1}}(\mathbf{v}')} \right\|_2 \right\|_2,$$

where the square root of a vector is applied element-wisely. Compared to the  $l_2$  (Euclidean) distance, the Hellinger distance includes the square root operation in its formula which emphasizes more on the peak values of distribution functions. As a result, a single fiber

voxel will be more similar to its single fiber neighbors than to its crossing fiber neighbors, so that the signals from crossing fiber neighbors will be down-weighted in its smoothing process. Similarly, a crossing fiber voxel will not be influenced too much by the signals from its single fiber neighbors. With the Hellinger distance, the boundary between (estimated) single fiber regions and crossing fiber regions will be more clearly defined.

### 3.2 Rescaling scheme

The proposed weighting scheme in Eq. (6), however, does not handle “extreme cases” very effectively and by “extreme cases” we mean either the already well-smoothed FOD estimates or still severely under-smoothed estimates. If the FOD estimate at voxel  $\mathbf{v}$  is already well-smoothed, when the neighborhood radius  $d_s$  increases, both the spatial weight  $\omega_{\text{loc},d_s}(\mathbf{v}, \mathbf{v}')$  and the similarity weight  $\omega_{\text{sim},d_s}(\mathbf{v}, \mathbf{v}')$  for  $\mathbf{v}' \in N_{d_s}(\mathbf{v})$  will tend to increase (the latter is due to the increased similarity of FOD estimates within the neighborhood). This can result in (potential) over-smoothing and increased bias in FOD estimation. On the other hand, if the FOD estimate at voxel  $\mathbf{v}$  is still under-smoothed, we expect it could benefit more from incorporating neighborhood information. However in such a case, even with increasing neighborhood radius  $d_s$ , the weight  $\omega_{d_s}(\mathbf{v}, \mathbf{v}')$  will not increase much since the similarity weight  $\omega_{\text{sim},d_s}(\mathbf{v}, \mathbf{v}')$  would still be small due to the large dissimilarities between the estimated FODs at voxel  $\mathbf{v}$  and those at its neighboring voxels. This can lead to (potential) under-smoothing and high variance in FOD estimation.

In the following, we propose a rescaling scheme for the dissimilarity measure to adjust for aforementioned scenarios. Specifically, at step  $s$ , we first find the smallest Hellinger distance between the estimated FOD at a voxel  $\mathbf{v}$  and the estimated FODs at its nearest neighboring voxels, which are the nearest four voxels (left, right, top, bottom) on a two-dimensional region or the nearest six voxels (left, right, top, bottom, front, end) on a three-dimensional region. We denote this minimum nearest-neighbor distance at step  $s$  as  $\text{MNN-Dist}_s(\mathbf{v}) := \min_{\mathbf{v}': \text{nearest neighbors of } \mathbf{v}} \text{Dist}_s(\mathbf{v}, \mathbf{v}')$ .

Since it is natural to assume that each voxel has at least one nearest neighbor that has a similar fiber configuration, a relatively large value of  $\text{MNN-Dist}_s(\mathbf{v})$  indicates under-smoothing and a relatively small value indicates adequate-smoothing or over-smoothing.

For a pre-specified small value  $\alpha > 0$ , let  $\text{MNN-Dist}_s^\alpha$  and  $\text{MNN-Dist}_s^{1-\alpha}$  denote the  $\alpha 100\text{th}$  and  $(1 - \alpha) 100\text{th}$  percentiles of  $\text{MNN-Dist}_s(\mathbf{v})$  across all voxels  $\mathbf{v}$ , respectively. The voxels with  $\text{MNN-Dist}_s(\mathbf{v}) > \text{MNN-Dist}_s^{1-\alpha}$  are then considered to be under-smoothed, and more aggressive further smoothing should be applied. On the other hand, the voxels with  $\text{MNN-Dist}_s(\mathbf{v}) < \text{MNN-Dist}_s^\alpha$  are considered to be well-smoothed, and less further smoothing should be applied. We investigate the effect of  $\alpha$  in Section 4 and find that setting  $\alpha = 15\%$  works well in practice.

The rescaling is then done as follows. Suppose for voxel  $\mathbf{v}$ ,  $\text{MNN-Dist}_s(\mathbf{v}) = \text{Dist}_s(\mathbf{v}, \mathbf{u})$ , where  $\mathbf{u}$  is one of the nearest neighbors of  $\mathbf{v}$ , then  $\text{Dist}_s(\mathbf{v}, \mathbf{u})$  is set to be  $\text{MNN-Dist}_s^{1-\alpha}$  if  $\text{MNN-Dist}_s(\mathbf{v}) > \text{MNN-Dist}_s^{1-\alpha}$ , and it is set to be  $\text{MNN-Dist}_s^\alpha$  if  $\text{MNN-Dist}_s(\mathbf{v}) < \text{MNN-Dist}_s^\alpha$ . Then all the other  $\text{Dist}_s(\mathbf{v}, \mathbf{v}')$ ,  $\mathbf{v}' \in N_{d_s}(\mathbf{v})$ ,  $\mathbf{v}' \neq \mathbf{u}$ , are rescaled (upward or downward) proportionally. More precisely, define the rescaling factor for voxel  $\mathbf{v}$  at step  $s$ :

$$\gamma_s(\mathbf{v}) := \min \left\{ \frac{\text{MNN-Dist}_s^{1-\alpha}}{\text{MNN-Dist}_s(\mathbf{v})}, 1 \right\} \cdot \max \left\{ \frac{\text{MNN-Dist}_s^\alpha}{\text{MNN-Dist}_s(\mathbf{v})}, 1 \right\},$$

and define the rescaled dissimilarity measure between the estimated FODs at voxels  $\mathbf{v}$  and  $\mathbf{v}'$  at step  $s$  as:

$$\widetilde{\text{Dist}}_s(\mathbf{v}, \mathbf{v}') := \gamma_s(\mathbf{v}) \cdot \text{Dist}_s(\mathbf{v}, \mathbf{v}').$$

The new weights at step  $s$  are then calculated as:

$$\omega_{d_s}(\mathbf{v}, \mathbf{v}') = \frac{K_{\text{loc}}(\|\mathbf{v} - \mathbf{v}'\|_2/d_s) K_{\text{sim}}(\gamma \cdot \widetilde{\text{Dist}}_s(\mathbf{v}, \mathbf{v}'))}{\sum_{\mathbf{v}' \in N_{d_s}(\mathbf{v})} K_{\text{loc}}(\|\mathbf{v} - \mathbf{v}'\|_2/d_s) K_{\text{sim}}(\gamma \cdot \widetilde{\text{Dist}}_s(\mathbf{v}, \mathbf{v}'))} \quad (7)$$

Since  $\gamma \cdot \widetilde{\text{Dist}}_s(\mathbf{v}, \mathbf{v}') = \gamma \cdot \gamma_s(\mathbf{v}) \cdot \text{Dist}_s(\mathbf{v}, \mathbf{v}')$ , the new weights from Eq. (7) are calculated in the same way as the weights from Eq. (6) with the smoothness parameter  $\gamma$  replaced by  $\gamma \cdot \gamma_s(\mathbf{v})$ . For the under-smoothed voxels, we have  $\text{MNN-Dist}_s(\mathbf{v}) > \text{MNN-Dist}_s^{1-\alpha}$ . So  $\gamma_s(\mathbf{v}) < 1$  and  $\gamma \cdot \gamma_s(\mathbf{v}) < \gamma$ , which means slower decay of the weights and more aggressive smoothing. On the other hand, for those already well-smoothed voxels, we have  $\text{MNN-Dist}_s(\mathbf{v}) < \text{MNN-Dist}_s^\alpha$ . So  $\gamma_s(\mathbf{v}) > 1$  and  $\gamma \cdot \gamma_s(\mathbf{v}) > \gamma$ , which means less aggressive smoothing.

### 3.3 Stopping rule

A well-thought stopping rule is essential to prevent over-smoothing. Our proposed stopping rule is also based on the minimum nearest-neighbor distance  $\text{MNN-Dist}_s(\mathbf{v})$  defined in the

previous section. The basic idea is to terminate the smoothing procedure for voxel  $\mathbf{v}$  when  $\text{MNN-Dist}_s(\mathbf{v})$  stops decreasing as the step index  $s$  increases. Specifically, when  $\min\{\text{MNN-Dist}_s(\mathbf{v}), \text{MNN-Dist}_{s-1}(\mathbf{v})\} \geq \text{MNN-Dist}_{s-2}(\mathbf{v})$ , we terminate the smoothing process for voxel  $\mathbf{v}$  and set  $\hat{\beta}_{d_{s'}}(\mathbf{v}) \equiv \hat{\beta}_{d_{s-2}}(\mathbf{v})$  for all  $s' \geq s - 1$ . The rationale behind this stopping rule is straightforward: when  $\text{MNN-Dist}_s(\mathbf{v})$  stops decreasing, the extent of similarity between voxel  $\mathbf{v}$  and its nearest neighbors is not increasing anymore, which means voxel  $\mathbf{v}$  has already been well-smoothed and thus the smoothing process for voxel  $\mathbf{v}$  should be terminated. In practice, the smoothing process for different voxels may stop at different steps, which accounts for heterogeneity in the degree of spatial homogeneity across different regions.

The computational costs of weights calculation and stopping rule checking are both much cheaper than the cost of FOD estimation. Hence, compared with the voxel-wise FOD estimation method, the NARM procedure costs at most  $S$  times more, where  $S$  is the pre-specified maximum number of smoothing steps. In fact, the cost is usually much less than  $S$  times in practice (usually around  $S/2$  times), since no FOD estimation is needed once the smoothing procedure is terminated according to the stopping rule.

### 3.4 Related work and comparison

Rao et al. (2016) proposed *Penalized Multiscale Adaptive Regression Model* (PMARM) for spatial and adaptive estimation of orientation distribution function (ODF – an alternative model for D-MRI data). As a general smoothing framework, PMARM can be adapted to FOD estimation. Same as NARM, PMARM also replaces the diffusion measurements at each voxel by the weighted average of diffusion measurements from “nearby” voxels, while adaptively updating the weights for nested neighborhoods with increasing radius, and using a stopping rule to avoid over-smoothing. However, PMARM has three major differences compared with NARM that render it less effective in FOD estimation.

First, in PMARM, the dissimilarity measure  $\text{Dist}_s(\mathbf{v}, \mathbf{v}')$  between two previously estimated objects is based on the  $l_2$  (Euclidean) distance, whereas in NARM, the Hellinger distance is used for calculating the dissimilarity measure. As pointed out in subsection 3.1, compared with the Hellinger distance, the  $l_2$  distance is less effective in quantifying the dissimilar-

ity between FODs which are smooth functions with none or a few distinct sharp peaks. Specifically, the  $l_2$  measure could lead to a misleadingly small distance between two FODs with one from a single-fiber voxel and the other from a crossing-fiber voxel, resulting in biased FOD estimation after smoothing. Second, PMARM does not have a rescaling mechanism for the similarity weight  $\omega_{\text{sim},d_s}(\mathbf{v}, \mathbf{v}')$ , which may lead to either over-smoothing or under-smoothing as discussed in subsection 3.2.

Finally, PMARM uses a global stopping criterion for all voxles, whereas NARM uses an adaptive criterion tailored for each voxel which is more effective in accounting for heterogeneity in the degree of spatial homogeneity (e.g., single-fiber region vs. crossing-fiber region). Since the stopping rule is a crucial component for a smoothing procedure, a simple yet effective stopping rule is a major advantage.

Specifically, at step  $s$ , let  $\text{Dist}_s(\mathbf{v})$  denote the  $l_2$  distance between previously estimated FOD  $\hat{\mathbf{f}}_{d_{s-1}}(\mathbf{v})$  and currently estimated FOD  $\hat{\mathbf{f}}_{d_s}(\mathbf{v})$ . In PMARM, for a pre-specified positive scalar  $c_s$ , if  $\text{Dist}_s(\mathbf{v}) > c_s$ , the smoothing procedure would be terminated and we set  $\hat{\beta}_{d_{s'}}(\mathbf{v}) = \hat{\beta}_{d_{s-1}}(\mathbf{v})$  for all  $s' \geq s - 1$  for voxel  $\mathbf{v}$ . Here the rationale is that, the significant change in the estimated FOD might be due to “bad” signals from some neighborhood voxels being incorporated. On the other hand, if  $\text{Dist}_s(\mathbf{v}) \leq c_s$ , the smoothing procedure is continued for voxel  $\mathbf{v}$ . In PMARM,  $c_s$  is set as  $c \cdot \chi_{(1)}^2(0.6/s)$ , where  $\chi_{(1)}^2(\alpha)$  is the upper  $\alpha 100\text{th}$  percentile of the  $\chi_{(1)}^2$  distribution, and  $c$  is a positive scalar, which is chosen to be the median of dissimilarity at step  $s = 0$ ,  $\text{Dist}_0(\mathbf{v}, \mathbf{v}')$ , across some preselected voxel pairs  $\mathbf{v}$  and  $\mathbf{v}'$ . Note that the threshold  $c_s$  only depends on the step index  $s$  and is not voxel-dependent.

A global stopping criterion such as the one used in PMARM may not work well for all voxels. This is because, for some voxels (e.g., single-fiber voxels), the voxel-wise FOD estimates are usually already quite good and the FOD estimates can become over-smoothed very quickly; and for some other voxels (e.g., crossing-fiber voxels), the voxel-wise FOD estimates usually are not as good and more smoothing steps are needed. On the contrary, the stopping rule in NARM is based on the minimum nearest-neighbor distance of each voxel and naturally adapts to the intrinsic spatial homogeneity of individual voxels.

Moreover, as pointed out by Rao et al. (2016), in practice it can be hard to specify a

good sequence of the thresholds  $c_s$ . Particularly, the hyper parameter  $c$  is very hard to choose and the synthetic experiments in Section 4 show that the results are indeed quite sensitive to the choice of  $c$ .

## 4 Synthetic experiments

In this section, we use extensive simulation studies based on two-dimensional and three-dimensional regions of interest (ROIs) with synthetic D-MRI data to evaluate the performance of our proposed NARM method, and to compare it with other FOD estimation methods including the voxel-wise SN-lasso method and the PMARM method.

### 4.1 Simulation setup

In ROIs, we simulate the noiseless diffusion weighted signals according to the spherical convolution model Eq. (1). For voxels with at least one fiber bundles, the true FOD function is constructed by a weighted summation of dirac functions:  $F(\theta, \phi) = \sum_{k=1}^K p_k \delta_{\theta_k, \phi_k}(\theta, \phi)$ ,  $\theta \in [0, \pi]$ ,  $\phi \in [0, 2\pi)$ , with  $p_k$  being the volume fraction of the  $k$ -th fiber bundle and  $(\theta_k, \phi_k)$  being the spherical coordinate of  $k$ -th fiber direction. In our simulation studies, we set  $p_1 = p_2 = 0.5$  for voxels with two fiber bundles. For voxels with zero fiber bundle (i.e., isotropic diffusion), the true FOD function is constant on the sphere:  $F(\theta, \phi) = 1/(4\pi)$ . The response function is built based on the single tensor model (Le Bihan & Warach 1995, Basser & Jones 2002, Mori 2007):  $R(\cos(\theta)) = S_0 \exp(-b(\lambda_1 \sin^2 \theta + \lambda_3 \cos^2 \theta))$ ,  $\theta \in [0, \pi]$ , where we set  $S_0 = 1$ ,  $b$ -value  $b = 1000s/mm^2$  or  $3000s/mm^2$ ,  $\lambda_1 = 10^{-3}mm^2/s$ , and the ratio between  $\lambda_3$  and  $\lambda_1$  as 10 for voxels with at least one fiber bundles and 1 for voxels with zero fiber bundle. We generate the noiseless diffusion weighted signals along  $n$  gradient directions, where the gradient directions are based on the icosphere meshes on the half-sphere and  $n$  is set to be either 41 or 81. Finally, we add independent Rician noise (Gudbjartsson & Patz 1995, Hahn et al. 2006) to the noiseless diffusion weighted signals to generate the observed diffusion weighted measurements. The *signal-to-noise ratio (SNR)* defined as  $S_0/\sigma$ , where  $\sigma$  is the Rician noise level, is set to be 20 throughout.

In the simulation experiments, we generate true fiber directions and their corresponding

observed diffusion weighted measurements on two-dimensional or three-dimensional voxel grids. These fiber directions are changing smoothly across voxels, and within each voxel, there is either one dominant fiber direction, two crossing fiber directions, or no fiber direction at all (i.e., isotropic diffusion). In 2D-ROI simulations, we conduct a comprehensive exploration of the FOD estimation methods, including the voxel-wise **SN-lasso** method (referred to as **SN-lasso**(voxel-wise)), the **NARM** method with different  $\alpha$  in weight rescaling (referred to as **NARM**( $\alpha = \alpha_0$ )), the **NARM** method with certain components missing (referred to as **NARM**(no stopping&rescaling), **NARM**(no stopping) and **NARM**(no rescaling), respectively), the **NARM** method with the stopping rule replaced by the one in **PMARM** (referred to as **NARM**( $\chi^2$ -stopping,  $c = c_0$ )), and the **PMARM** method with different  $c$  in the stopping criterion (referred to as **PMARM**( $c = c_0$ )). We also include the voxel-wise **SN-lasso** method applied to the noiseless diffusion signals (referred to as **SN-lasso**(noiseless)) as the gold standard. In 3D-ROI simulations, we only focus on a small set of FOD estimation methods which are representative of the aforementioned methods. The number of fiber directions and the directions themselves are then estimated and extracted from the estimated FODs by using the peak detection algorithm proposed in Yan et al. (2018).

We use a variety of numerical metrics to examine the performance of each method. These include: (1) The proportions of voxels where the number of detected fiber bundles are either correct, over-estimated or under-estimated, reported under “Co.,” “Ov.” and “Un.” respectively in the tables. (2) Among the “correct” voxels, the median angular error between the identified fiber direction(s) and true fiber direction(s), shown under “Err.” in the tables. (3) The mean and standard deviation (across all voxels in the ROI) of the Hellinger distance between the estimated FOD and the true FOD (projected onto an SH basis with  $l_{\max} = 8$ ), and between the estimated FOD and the estimated FOD from noiseless signals. They are shown under “Mean H-dist.” and “SD H-dist.” in the tables.

## 4.2 2D ROI simulation I

In the first simulation, we generate two fiber bundles on a  $10 \times 10$  2D voxel grid with 72 one-fiber voxels and 28 two-fiber voxels. One fiber bundle runs from the top left to the bottom right, and the other runs from the top right to the bottom left, with the crossing-fiber region



in the middle of the ROI. Figure 1(a) shows the true FODs represented by  $l_{\max} = 8$  SH basis on this ROI. We set the  $b$ -value  $b = 1000s/mm^2$  and the number of gradient directions  $n = 41$ . In some real D-MRI studies such as HCP, the  $b$ -values and the numbers of gradient directions are larger than the setting here, leading to easier/better FOD estimation. Since the goal of this simulation is to examine the performance of various methods and reveal usefulness of each component in the smoothing procedure, this relatively challenging setting could help with better understanding of strength and weakness of each method. We refer to this simulation as the **2D ROI simulation I**.

We examine the performance of FOD estimation methods listed in Section 4.1. Specifically, we set  $\alpha_0 \in \{0.10, 0.15, 0.20\}$  in  $\text{NARM}(\alpha = \alpha_0)$ ,  $c_0 \in \{3, 4\}$  in  $\text{NARM}(\chi^2\text{-stopping}, c = c_0)$ , and  $c_0 \in \{0.10, 0.15, 0.20\}$  in  $\text{PMARM}(c = c_0)$ . Moreover, we set  $\gamma = 2$  in  $K_{\text{sim}}(u) = \exp(-\gamma u^2)$  for  $\text{NARM}$  and  $\gamma = 20$  for  $\text{PMARM}$  (adjusted for scale difference). The results show that FOD estimation is not very sensitive to the choice of  $\alpha$  when it varies between 0.1 and 0.2. On the other hand, FOD estimation is quite sensitive to the choice of  $c$ . Indeed here we have already preselected a set of  $c$  which lead to relatively good results. In practice,  $c$  is not easy to specify and the  $c$  specification approach described in Rao et al. (2016) is somewhat ad-hoc.

Figure 1(b)-(f) present the estimated FODs on this ROI. In general, the FOD estimates with smoothing procedure (Figure 1(c)-(f)) outperform the voxel-wise FOD estimates (Figure 1(b)) in terms of recovering the fiber configurations especially in the crossing-fiber region. The  $\text{NARM}$  estimates without stopping rule and weight rescaling (Figure 1(d)) tend to be over-smoothed, where the boundary between the single-fiber region and the crossing-fiber region is somewhat blurred. Compared with the  $\text{PMARM}$  estimates (Figure 1(e)(f)), the  $\text{NARM}$  estimates (Figure 1(c)) perform better in reconstructing the peak directions. For example, only the  $\text{NARM}$  estimates could successfully recover the crossing fiber structure in the voxel with coordinates (6, 9) (assuming the coordinates of the voxel in the bottom left is (1, 1)). This is a particularly challenging case due to the small crossing angle and its boundary location between the single-fiber region and crossing-fiber region. Take the single-fiber voxels (1, 6) and (10, 6) as another example. The  $\text{NARM}$  method leads to much less noisy estimates than the  $\text{PMARM}$  method does, where the  $\text{PMARM}$  estimates would lead

to wrong identification of these two single-fiber voxels as crossing-fiber voxels.

Table 1 and Table S.1 (of the Supplementary Material) present numerical metrics of FOD estimation performance by using the success rate&angular error and the Hellinger distance, respectively, where detailed descriptions of these metrics can be found in Section 4.1. We can see that the **NARM** estimates are not very sensitive to the choice of  $\alpha$  (the proportion that defines the “extreme cases” for weight rescaling), and  $\alpha = 0.15$  performs the best given that it has the smallest median angular error for 2-fiber voxels. Both tables reveal that the **NARM** estimates substantially reduce the failure rates, median angular errors and mean Hellinger distances compared to the voxel-wise **SN-lasso** estimates, indicating that **NARM** is able to effectively exploit spatial homogeneity and reduce noise for better peak detection and direction estimation. Compared with the **PMARM** estimates with three choices of  $c$  values in the stopping rule, **NARM** outperforms all of three given its perfect success rates for both 1-fiber and 2-fiber voxels and its smaller mean Hellinger distances. **PMARM** appears to suffer from blurred boundaries between the single-fiber region and the crossing-fiber region due to its relatively high proportion of over-estimated 1-fiber voxels and under-estimated 2-fiber voxels. Finally, if the stopping rule is not implemented, the **NARM** estimates would have significantly lower successful rates and larger angular errors for 1-fiber voxels due to over-smoothing. If we replace the proposed stopping rule in **NARM** by the stopping rule from **PMARM** (referred to as  $\chi^2$ -stopping), then it is less effective in distinguishing the single-fiber region and crossing-fiber region. In conclusion, the proposed stopping rule in **NARM** not only leads to better estimation, it is also easier to use in practice since there is no “parameter” that needs to be specified.

Figure 1: **2D ROI simulation I**: FOD estimates. (a) True FODs in SH basis with  $l_{\max} = 8$ ; (b) SN-lasso (voxel-wise) estimates; (c) NARM ( $\alpha = 0.15$ ) estimates; (d) NARM (no stopping&rescaling) estimates; (e) PMARM ( $c = 0.15$ ) estimates; (f) PMARM ( $c = 0.20$ ) estimates.

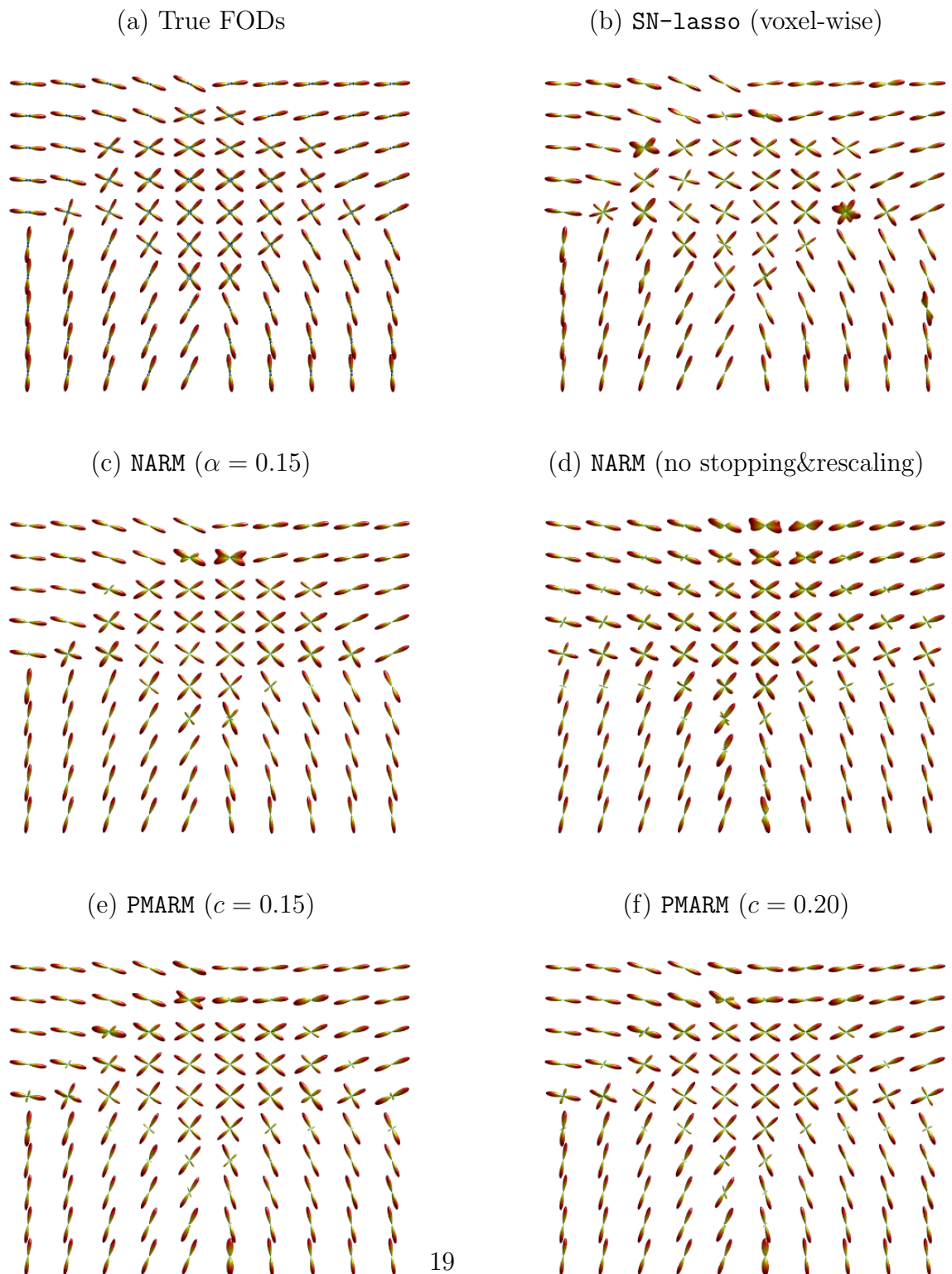


Table 1: **2D ROI simulation I**: Success rate and angular error.

Estimator	1-Fiber		2-Fiber	
	Co./Ov./Un.	Err.	Co./Ov./Un.	Err.
SN-lasso(noiseless)	1.00/0.00/0.00	1.55	1.00/0.00/0.00	1.00
SN-lasso(voxel-wise)	1.00/0.00/0.00	2.62	0.78/0.18/0.04	8.51
NARM( $\alpha = 0.10$ )	1.00/0.00/0.00	2.61	1.00/0.00/0.00	3.81
NARM( $\alpha = 0.15$ )	1.00/0.00/0.00	2.61	1.00/0.00/0.00	3.59
NARM( $\alpha = 0.20$ )	1.00/0.00/0.00	2.61	1.00/0.00/0.00	3.72
NARM(no stopping&rescaling)	0.81/0.19/0.00	5.34	0.96/0.04/0.00	3.09
NARM(no stopping)	0.76/0.24/0.00	4.62	0.96/0.04/0.00	3.04
NARM(no rescaling)	1.00/0.00/0.00	2.61	1.00/0.00/0.00	3.81
NARM( $\chi^2$ -stopping, $c = 3$ )	0.97/0.03/0.00	2.69	0.93/0.03/0.04	3.72
NARM( $\chi^2$ -stopping, $c = 4$ )	0.94/0.06/0.00	2.72	0.96/0.00/0.04	3.34
PMARM( $c = 0.15$ )	0.93/0.07/0.00	2.53	0.96/0.00/0.04	4.08
PMARM( $c = 0.20$ )	0.92/0.08/0.00	2.61	0.96/0.00/0.04	3.44
PMARM( $c = 0.25$ )	0.89/0.11/0.00	2.64	0.96/0.00/0.04	3.44

### 4.3 2D ROI simulation II

The second simulation involves a 2D ROI where two fiber bundles are crossing on a  $10 \times 10$  grid. There are 22 zero-fiber (i.e., isotropic) voxels, 66 one-fiber voxels and 12 two-fiber voxels. The true FODs represented by  $l_{\max} = 8$  SH basis are shown in Figure 2(a). We still set the  $b$ -value  $b = 1000s/mm^2$  and the number of gradient directions  $n = 41$ . This simulation is referred to as **2D ROI simulation II**.

The results are reported in Figure 2, Table 2, and Table S.2 (of the Supplementary Material). As can be seen from Figure 2, the NARM estimates (Figure 2(c)) and the PMARM estimates with  $c = 0.05$  (Figure 2(e)) correctly identify more zero-fiber voxels than the voxel-wise SN-lasso estimates (Figure 2(b)). Moreover, NARM outperforms PMARM given its perfect success rate and much lower median angular error on the crossing fiber-region as

well as its lower mean Hellinger distance. Note that the **PMARM** estimates with  $c = 0.10$  (Figure 2(f)) perform much worse than the **PMARM** estimates with  $c = 0.05$  (Figure 2(e)) in terms of successful rate on the zero-fiber region, indicating sensitivity of the **PMARM** results in the choice of  $c$  and the difficulty in  $c$  specification for **PMARM** in practice. Finally, removing stopping rule and weight rescaling from **NARM** (Figure 2(d)) would result in spurious peaks in the zero-fiber region (due to over-smoothing with the neighboring 1-fiber/2-fiber voxels). Replacing the proposed stopping rule in **NARM** by the  $\chi^2$  stopping rule from **PMARM** would worsen the success rate of peak detection in all three regions.

Figure 2: **2D ROI simulation II**: FOD estimates. (a) True FODs in SH basis with  $l_{\max} = 8$ ; (b) SN-lasso (voxel-wise) estimates; (c) NARM ( $\alpha = 0.15$ ) estimates; (d) NARM (no stopping&rescaling) estimates; (e) PMARM ( $c = 0.05$ ) estimates; (f) PMARM ( $c = 0.10$ ) estimates.

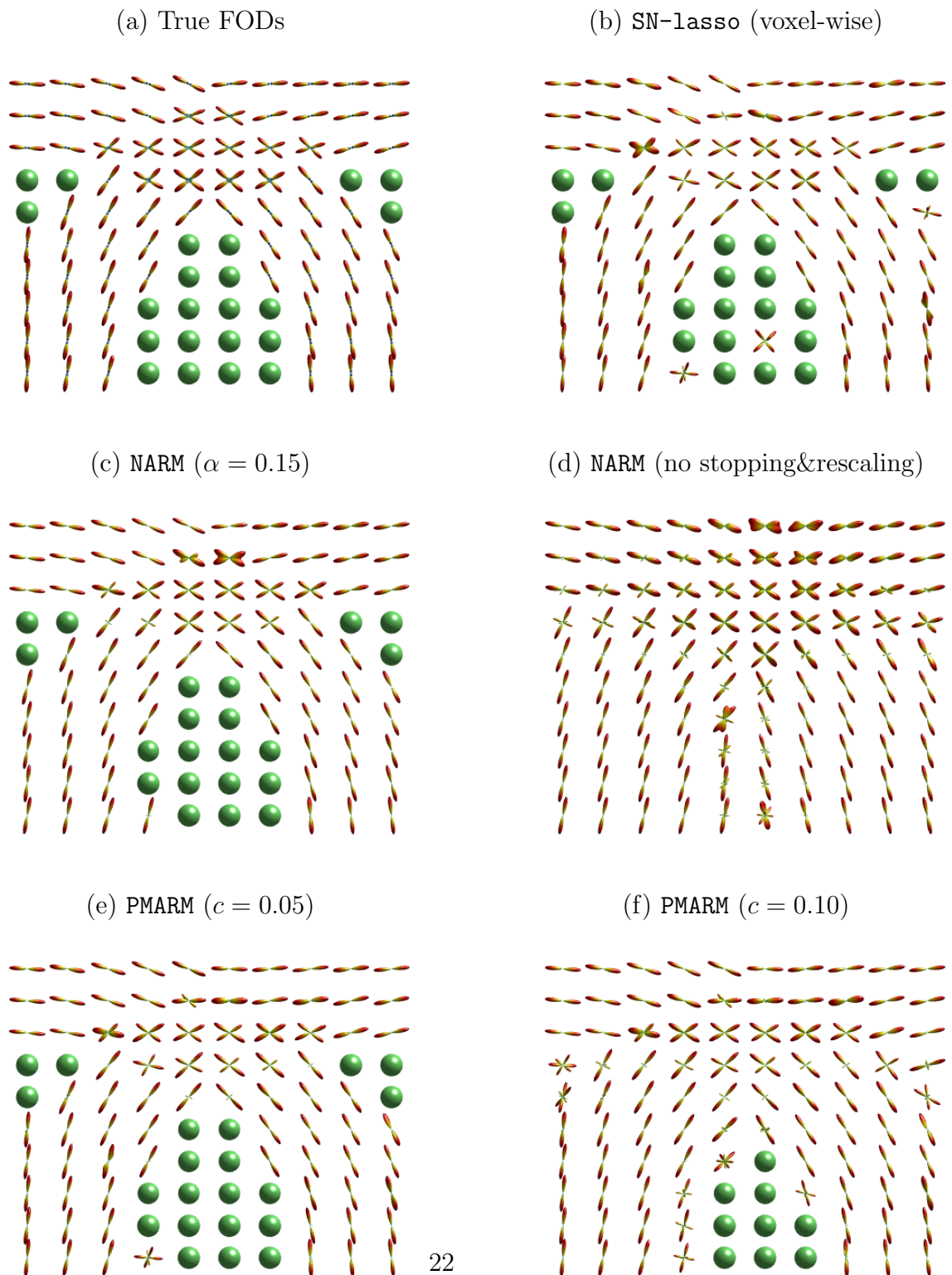


Table 2: **2D ROI simulation II**: Success rate and angular error.

Estimator	0-Fiber	1-Fiber		2-Fiber	
	Co./Ov.	Co./Ov./Un.	Err.	Co./Ov./Un.	Err.
SN-lasso(noiseless)	1.00/0.00	1.00/0.00/0.00	1.92	1.00/0.00/0.00	1.00
SN-lasso(voxel-wise)	0.86/0.14	1.00/0.00/0.00	2.72	0.92/0.00/0.08	8.88
NARM( $\alpha = 0.10$ )	0.95/0.05	1.00/0.00/0.00	2.93	1.00/0.00/0.00	4.76
NARM( $\alpha = 0.15$ )	0.95/0.05	1.00/0.00/0.00	2.86	1.00/0.00/0.00	4.76
NARM( $\alpha = 0.20$ )	0.95/0.05	0.98/0.02/0.00	2.86	1.00/0.00/0.00	4.76
NARM(no stopping&rescaling)	0.00/1.00	0.79/0.21/0.00	4.00	1.00/0.00/0.00	4.37
NARM(no stopping)	0.68/0.32	0.79/0.21/0.00	4.18	1.00/0.00/0.00	3.70
NARM(no rescaling)	0.95/0.05	1.00/0.00/0.00	2.93	1.00/0.00/0.00	4.76
NARM( $\chi^2$ -stopping, $c = 2$ )	0.73/0.27	0.97/0.03/0.00	2.48	0.92/0.00/0.08	5.69
NARM( $\chi^2$ -stopping, $c = 3$ )	0.73/0.27	0.95/0.05/0.00	2.57	0.92/0.00/0.08	4.28
NARM( $\chi^2$ -stopping, $c = 4$ )	0.73/0.27	0.94/0.06/0.00	2.57	0.92/0.00/0.08	3.70
PMARM( $c = 0.05$ )	0.95/0.05	1.00/0.00/0.00	2.57	0.92/0.00/0.08	6.87
PMARM( $c = 0.10$ )	0.41/0.59	0.97/0.03/0.00	2.55	0.92/0.00/0.08	6.41

#### 4.4 3D ROI simulation

In the third simulation, we generate two fiber bundles on a  $10 \times 10 \times 5$  3D voxel grid, where there are 52 zero-fiber voxels, 163 one-fiber voxels and 285 two-fiber voxels. We consider two  $b$ -values at  $b = 1000s/mm^2$  and  $3000s/mm^2$ , respectively, and the number of gradient directions  $n = 41$ . We refer to this simulation as the **3D ROI simulation**,

Based on results from the 2D ROI simulations, here we focus on a subset of FOD estimation methods including the voxel-wise SN-lasso method, the NARM method with  $\alpha = 0.15$ , the NARM method without stopping and rescaling, and the PMARM method with  $c = 0.05$  and  $c = 0.10$ . As mentioned earlier, in NARM, we set  $\gamma = 2$  in the similarity kernel  $K_{\text{sim}}(u) = \exp(-\gamma u^2)$  when  $b = 1000s/mm^2$ ; and  $\gamma = 4$  when  $b = 3000s/mm^2$ .

In the main text, we only report part of the simulation results when  $b = 1000s/mm^2$  and defer other results to Sections S.1.3 and S.1.4 of the Supplementary Material. We

can see from Figure 3, Table 3, and Table S.3 (of the Supplementary Material) that the **NARM** method leads to the most accurate estimates of FODs: It has nearly perfect success rates among 0-fiber, 1-fiber and 2-fiber voxels, the lowest median angular errors, and the smallest mean Hellinger distance. Among the other methods, the voxel-wise **SN-lasso** method performs poorly in terms of peak detection in the crossing-fiber region, the **PMARM** methods have worse success rate and angular error, and the **NARM** method without stopping and rescaling tends to results in spurious peaks in the zero-fiber and single-fiber voxels.

We use the tractography results presented in Figure S.1 to further illustrate and justify our findings. To reconstruct the fiber trajectories, we use the peak detection algorithm (Yan et al. 2018) to extract peaks from the estimated FODs and then apply the deterministic tracking algorithm (Wong et al. 2016) to the extracted peaks. In Figure S.1, the fiber tracts are colored coded with red for left-to-right, green for up-to-down and blue for into-to-out-of-page. We also report the total number of fiber tracts and the median of fiber lengths in Figure S.1. As can be seen from Figure S.1, the tracking result based on the **NARM** method (Figure S.1(c)) appears to be the closest to the underlying truth (Figure S.1(a)), where it shows very clear fiber crossing region with almost no redundant fiber tracts. On the contrary, the tracking result based on the voxel-wise **SN-lasso** method (Figure S.1(b)) are very messy especially in the crossing-fiber region. Moreover, the small value of its median fiber length (4.11) is likely due to incoherence of fiber directions extracted from its estimated FODs. Moreover, the fiber tracking results based on the two **PMARM** methods with  $c = 0.05$  and  $c = 0.10$  (Figure S.1(e)(f)) produce visually noisy reconstruction of fiber tracts. Finally, Figure S.1(d) shows that many spurious fiber tracts are generated by the **NARM** method without stopping and rescaling.

For  $b$ -value  $b = 3000s/mm^2$ , **NARM** again has visually the best FOD estimates and fiber tracking results, and the highest success rates in 0-fiber, 1-fiber and 2-fiber regions. See Section S.1.4 of the Supplementary Material for more details. Moreover, as expected the FOD estimation results from  $b$ -value at  $3000s/mm^2$  are generally better than those from  $b$ -value at  $1000s/mm^2$ .



Figure 3: **3D ROI simulation:** FOD estimates on  $z$ -slice 2. (a) True FODs in SH basis; (b) SN-lasso (voxel-wise) estimates; (c) NARM ( $\alpha = 0.15$ ) estimates; (d) NARM (no stopping&rescaling) estimates; (e) PMARM ( $c = 0.05$ ) estimates; (f) PMARM ( $c = 0.10$ ) estimates.

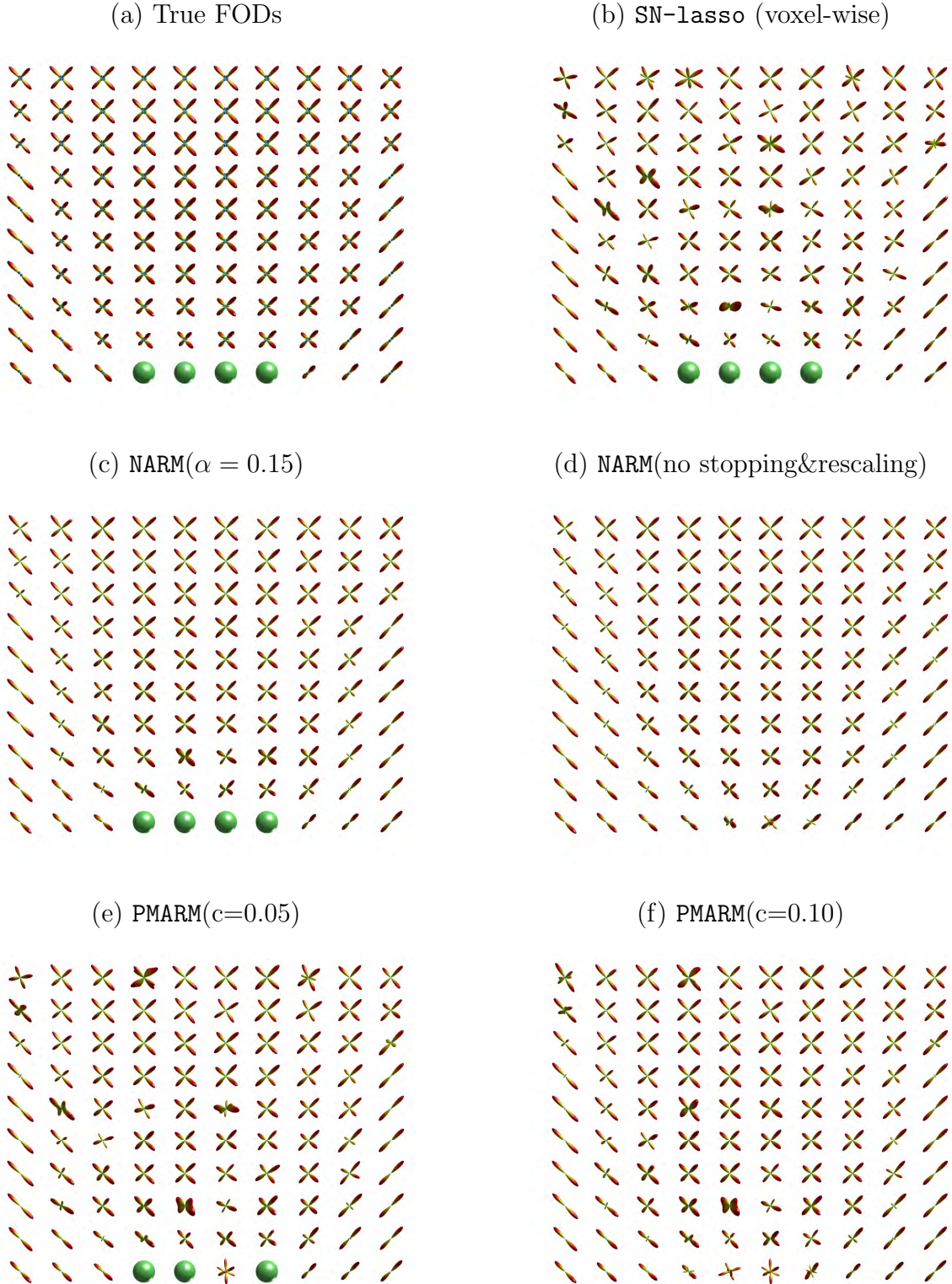


Table 3: **3D ROI simulation**: Success rate and angular error.

Estimator	0-Fiber	1-Fiber		2-Fiber	
	Co./Ov.	Co./Ov./Un.	Err.	Co./Ov./Un.	Err.
SN-lasso(noiseless)	1.00/0.00	1.00/0.00/0.00	1.61	1.00/0.00/0.00	1.77
SN-lasso(voxel-wise)	0.94/0.06	1.00/0.00/0.00	2.47	0.84/0.15/0.01	6.75
NARM( $\alpha = 0.15$ )	0.96/0.04	0.98/0.02/0.00	2.35	1.00/0.00/0.00	3.31
NARM(no stopping&rescaling)	0.13/0.87	0.75/0.25/0.00	3.27	1.00/0.00/0.00	2.74
PMARM( $c = 0.05$ )	0.90/0.10	0.95/0.05/0.00	2.63	0.94/0.06/0.00	3.93
PMARM( $c = 0.10$ )	0.40/0.60	0.90/0.10/0.00	2.81	0.97/0.03/0.00	3.42

## 4.5 Summary

We observe the following from the **2D ROI simulation I & II** and the **3D ROI simulation**. First, the FOD estimation methods with spatial smoothing outperform the voxel-wise SN-lasso method, especially in crossing-fiber regions. Second, compared with PMARM (with the best choice of the stopping rule parameter  $c$  based on ground truth), the NARM method is able to estimate FODs with more accurate peak directions, which leads to more faithful reconstruction of the fiber tracts. Third, an appropriate stopping rule is crucial for adaptive smoothing methods such as NARM and PMARM. Without stopping, the estimates could be over smoothed; while stopping too early could lead to high variability. The proposed stopping rule (including weight rescaling) for NARM is effective as well as insensitive to the choice of the hyper-parameter  $\alpha$ . In contrast, the stopping rule in PMARM is highly sensitive to the hyper-parameter  $c$ , making it hard to use in practice.

## 5 Real D-MRI data experiments

In this section, we evaluate the performance of NARM and SN-lasso using the test-retest data from the WU-Minn Human Connectome Project (HCP) (Essen et al. 2013). The data set consists of Eddy-current-corrected 3T D-MRI test-retest data from 36 healthy young adults, with age ranging from 22 to 35. The D-MRI measurements were taken at three

different  $b$ -values ( $1,000s/mm^2$ ,  $2,000s/mm^2$ ,  $3,000s/mm^2$ ) on a  $145 \times 174 \times 145$  grid with voxel size  $1.25 \times 1.25 \times 1.25mm^3$ . For our analysis, we use the D-MRI measurements with  $b$ -value =  $3,000s/mm^2$ . We focus on a region at the crossing of two major white matter fiber tracts, namely, the *Corticospinal Tract (CST)* and *Superior Longitudinal Fasciculus (SLF)* (Figure 5).

The D-MRI data were downloaded from the HCP database, *ConnectomeDB*, which have already gone through basic quality control and minimal preprocessing steps including intensity normalization, EPI distortion correction, Eddy current correction, Gradient nonlinearity correction, registration of the mean  $b_0$  image (T2w image) to the native volume T1w image, and transformation of diffusion data, gradient deviation, and the gradient directions to the *structural space (T1w space)* (Glasser et al. 2013). Moreover, the HCP D-MRI data have already been co-registered to the T1w space. We performed additional processing steps using the T1w and T2w images as described below. We utilized the software *FSL* version 6.0.0 (Jenkinson et al. 2012), and R packages *fslr* (Muschelli et al. 2015) and *neurohcp* (Muschelli 2018) from the *neuroconductor* repository.

The (original) T1w image contained both skull and the brain, so we first applied the T2w extracted binary brain mask provided by HCP to the T1w image to obtain the T1w extracted brain image. We then used the T1w extracted brain image and the *FAST* segmentation algorithm (Zhang et al. 2001) in *FSL* to classify each voxel to three different tissue types, namely, CSF–cerebrospinal fluid, GM–grey matter, WM–white matter. By doing so, we created a *white-matter mask*. Hereafter, the voxels within the white-matter mask were referred to as the *white-matter voxels*. Finally, the T1w images were registered to a standard space, *MNI152-T1 2mm* (<http://www.bic.mni.mcgill.ca/ServicesAtlases/HomePage>), by the *FSL* registration tools FLIRT (Jenkinson et al. 2002) (for initial linear registration) and FNIRT (Woolrich et al. 2009) (for subsequent nonlinear registration).

We selected a region containing the crossing fibers of the *Corticospinal Tract (CST)* and *Superior Longitudinal Fasciculus (SLF)* on the MNI152-T1 template space. We used *FSLeyes* (McCarthy 2020) and the *JHU White-Matter Tractography Atlas* (Wakana et al. 2007, Hua et al. 2008) to create the ROI masks in the left hemispheres for both the test and retest D-MRI scans. The ROI was defined as the voxels within X: -40 – -22, Y: -30

– -12, Z: 22 – 40 in the MNI 152 space, totaling 729 voxels (Figure 4 top panel). We further used binary masks from *AutoPtx* (de Groot et al. 2013) for streamline selection to dissect the SLF and the CST from the initial tractography results (Figure 5). We used the inverse transformation derived from the registration step to move the masks from the template MNI 152 space back to each subject’s native space (Figure 4 bottom panel). In the subject’s native space, the numbers of voxel within this ROI in the test and retest scans have the mean (standard deviation) 3906.114 (493.0) and 3912.257 (477.5), respectively. The paired difference of the numbers of voxels in the test and retest scans has a 95% confidence interval of (-32.134, 19.848).

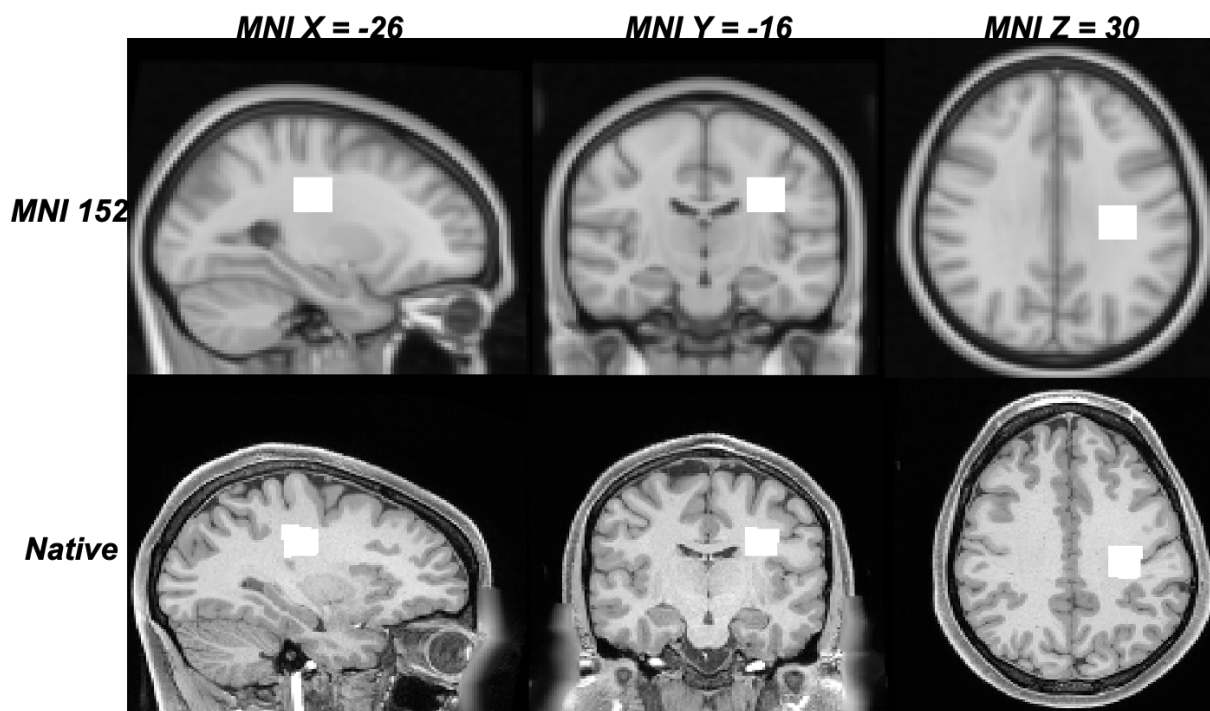


Figure 4: **Selected ROI.** Top: white box in the MNI 152 template space; Bottom: white region in the native space of one subject

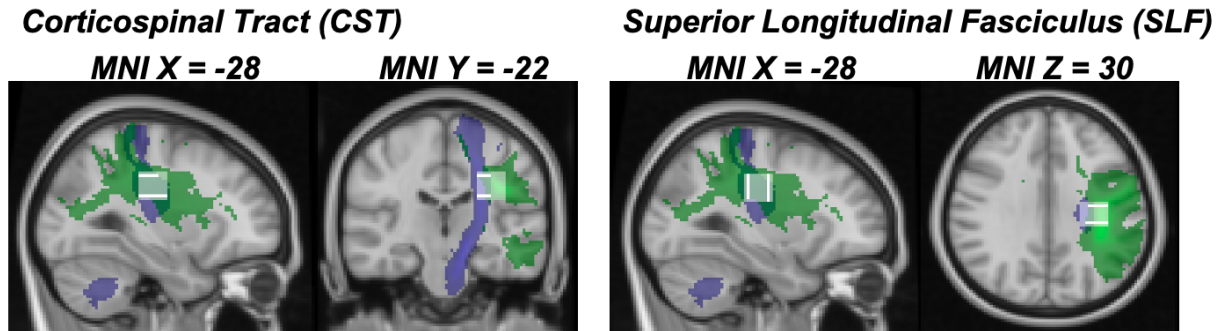


Figure 5: **ROI and streamline selection masks:** Green-color region corresponds to the left SLF; Blue-color region corresponds to the left CST; Transparent box indicates the selected ROI; White-color strips indicate the streamline selection masks.

We first estimated the FODs for the white-matter voxels within the ROI masks on each subject’s native space. To estimate the response function  $R(\cdot)$  in the FOD model (Eq. (1)), we followed the procedure outlined in Yan et al. (2018). First, we fitted the single tensor model for every white-matter voxel. We identified those with an FA value greater than 0.8 and the ratio between the two smaller eigenvalues of the estimated diffusion tensor less than 1.5 as having a single dominant fiber bundle. The median of the leading eigenvalues and the minor eigenvalues across these voxels are denoted by  $\bar{\lambda}$  and  $\underline{\lambda}$ , respectively. The response function is specified as:

$$R(\cos(\theta)) := S_0 \exp^{-b(\bar{\lambda} \cos^2 \theta + \underline{\lambda} \sin^2 \theta)}, \quad \theta \in [0, \pi].$$

Finally, we normalized the DWI measurements at each voxel by the mean intensity of the 6  $b_0$  images at that voxel and set  $S_0 = 1$  in the response function. (See Section S.2.1 for definitions of the single tensor model and FA value.)

We then obtained NARM estimates for the white-matter voxels within the ROI masks using SH and SN basis functions with  $l_{\max} = 8$  and  $j_{\max} = 3$ , respectively. We set the parameters in NARM as  $\gamma = 4$ ,  $\alpha = 0.15$ ,  $r = 1.15$ , and  $S = 6$ . The peak directions of the estimated FODs are extracted by a *peak detection algorithm* (Yan et al. 2018). These are then used as inputs in the deterministic tracking algorithm *DiST* (Wong et al. 2016) for fiber tracts reconstruction. And then, streamlines for CST and SLF are selected by using the streamline selection masks, which are registered in each subject’s native space. (Figure

5).

In the following, we analyze and compare the reconstruction results of **NARM** and **SN-lasso** (i.e., **NARM** at step 0 without spatial smoothing). Figures 6 and 7 illustrate the reconstructed streamlines for two different subjects across the entire ROI under three scenarios: 1) before selection (left panel), 2) after selection using CST masks (middle panel), 3) after selection using SLF masks (right panel). Notably, the bottom panels, which describe streamlines based on **NARM** FOD estimates, show tightly clustered, smoothly curved streamlines, compared to the top panels representing streamlines based on **SN-lasso** FOD estimates. We report the number of reconstructed streamlines from the test and re-test scans for both **NARM** and **SN-lasso** in Table 4. The table presents the average and standard deviation across all 36 subjects. Additionally, Figure 8 displays a scatter plot comparing the re-test results against the test results. **NARM** generates a higher number of streamlines than **SN-lasso** across the entire ROI and the SLF region. Conversely, **SN-lasso** produces more streamlines in the CST region. Furthermore, **NARM** has a larger intraclass correlation coefficient (ICC) between the number of the reconstructed streamlines based on test and re-test scans. **NARM** demonstrates a larger ICC for both the entire ROI and CST region, indicating greater consistency between the two scans. But, for the SLF region, **SN-lasso** exhibits a slightly larger ICC. In conclusion, the **NARM** reconstruction results present streamlines that are more realistic and consistent between test and re-test scans.

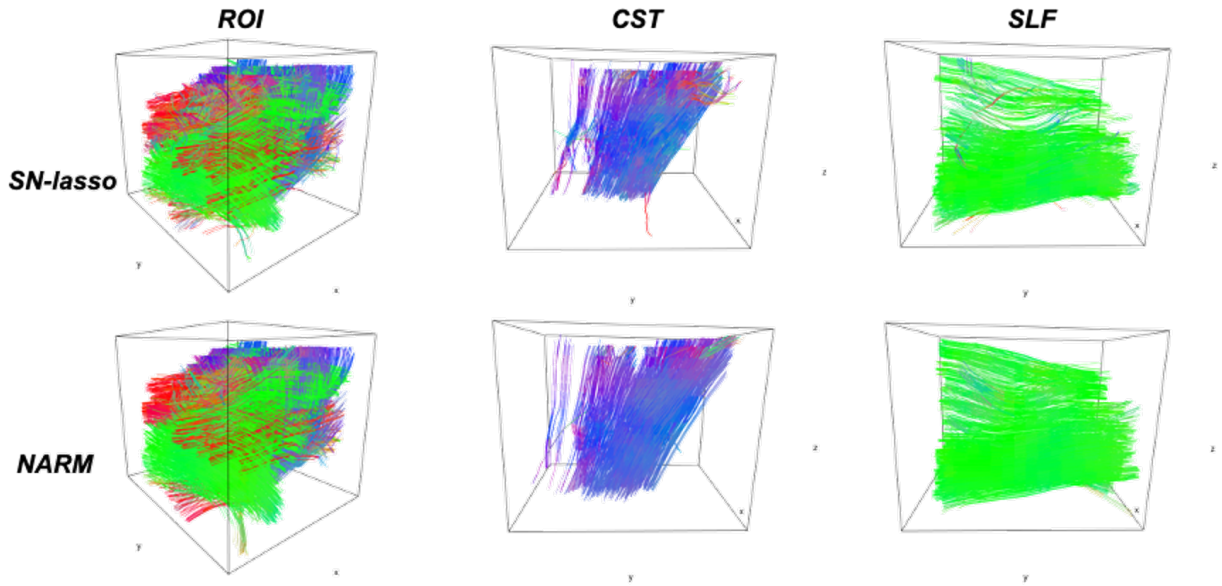


Figure 6: **Reconstructed fiber tracts for subject 1.** Left: on the entire ROI before streamline selection; Middle: CST streamline selection; Right: SLF streamline selection

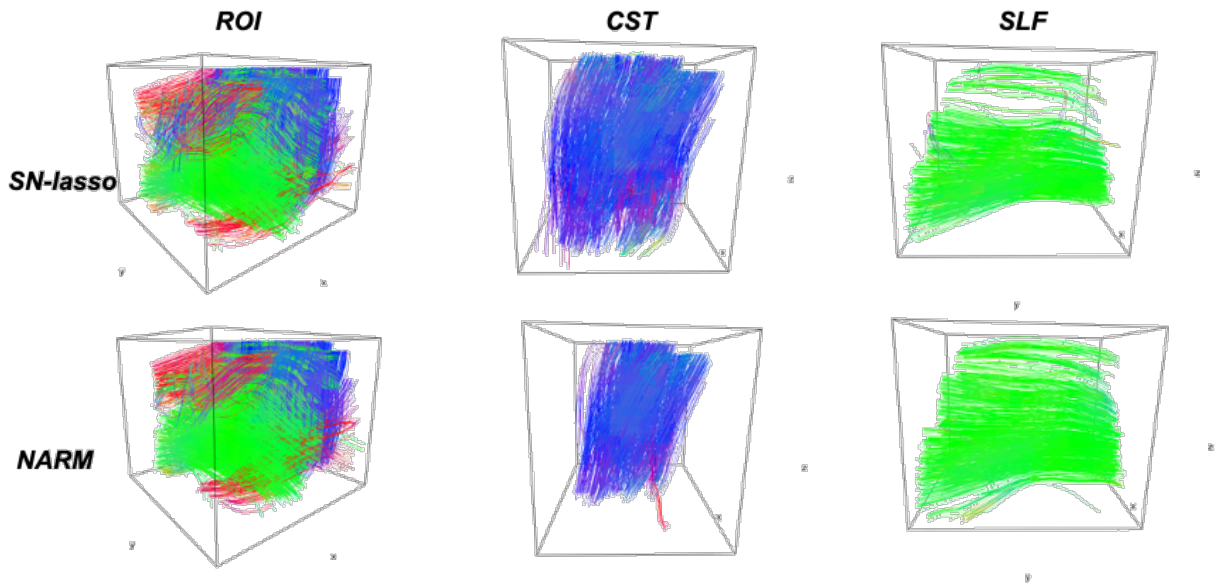


Figure 7: **Reconstructed fiber tracts for subject 2.** Left: on the entire ROI before streamline selection; Middle: CST streamline selection; Right: SLF streamline selection

Table 4: Number of reconstructed streamlines from test and retest scans.

Total number of Streamlines		ROI		SLF		CST	
		SN-lasso	NARM	SN-lasso	NARM	SN-lasso	NARM
Test	Mean	4500	4963	755	834	750	734
	SD	827.61	899.021	108.38	211.06	129.61	127
Retest	Mean	4574	5012	749	853	754	715
	SD	749.93	792.96	169.91	177.66	127.13	129.37
Intraclass Correlation		0.88	0.93	0.91	0.87	0.71	0.77

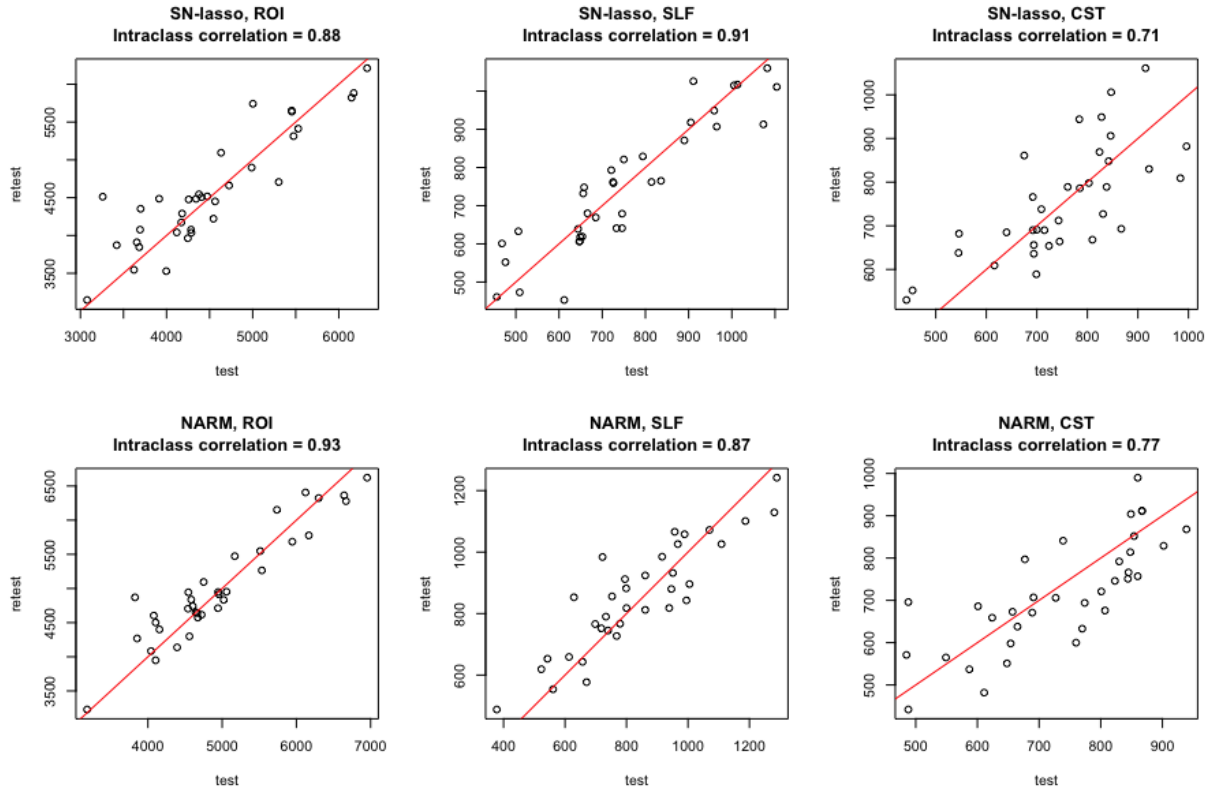


Figure 8: Scatter plots of re-test result vs. test result in the number of reconstructed streamlines. Left: on the entire ROI before streamline selection; Middle: SLF streamline selection; Right: CST streamline selection.



## 6 Discussion

In this paper, we propose a *Nearest-neighbor Adaptive Regression Model* (**NARM**) to adaptively estimate the FODs across all voxels using D-MRI data. **NARM** incorporates spatial constraint in D-MRI data by adaptively borrowing information from neighboring voxels and by doing so improves FOD estimation compared with voxel-wise method without spatial smoothing. Moreover, **NARM** outperforms an existing spatial smoothing procedure **PMARM** (Rao et al. 2016) thanks to three innovations: the use of Hellinger distance in FOD similarity measure makes FODs with different peak values more distinguishable; the weight rescaling scheme effectively handles “extreme cases” in smoothing; and the minimum nearest-neighbor distance based stopping rule is easy to implement in practice and is effective in preventing over-smoothing.

Experimental results on synthetic data demonstrate that **NARM** results in better FOD estimation than the voxel-wise **SN-lasso** method and the **PMARM** method. Consequently, **NARM** leads to more accurate and less noisy fiber orientation detection, and more coherent and smoother fiber tracking results. When applied to the HCP test-retest D-MRI data, the **NARM** estimates lead to more biologically sensible and interpretable tractography results compared to the voxel-wise **SN-lasso** method.

One direction for future research is to further improve the dissimilarity measure between FODs in weight calculation. Although the Hellinger distance is able to better identify differences in peak values between two FODs than the  $l_2$  distance, it is not very sensitive to peak direction shifts. A location-aware distance measure between density functions, for example the earth-mover distance, is expected to be a more effective dissimilarity measure.

## Acknowledgement

The authors gratefully acknowledge the following support: UCD Dissertation Year Fellowship (JLY), NIH 1R01EB021707 (JLY and JP), NSF-DMS-1148643 (JP) and NSF-DMS-1915894 (JP, SYH).

## References

- Basser, P. J. & Jones, D. K. (2002), ‘Diffusion-tensor mri: theory, experimental design and data analysis—a technical review’, *NMR in Biomedicine* **15**(7-8), 456–467.
- Basser, P. J., Mattiello, J. & LeBihan, D. (1994), ‘Mr diffusion tensor spectroscopy and imaging’, *Biophysical journal* **66**(1), 259–267.
- Basser, P. J., Pajevic, S., Pierpaoli, C., Duda, J. & Aldroubi, A. (2000), ‘In vivo fiber tractography using dt-mri data’, *Magnetic resonance in medicine* **44**(4), 625–632.
- Becker, S., Tabelow, K., Mohammadi, S., Weiskopf, N. & Polzehl, J. (2014), ‘Adaptive smoothing of multi-shell diffusion weighted magnetic resonance data by mspos’, *NeuroImage* **95**, 90–105.
- Becker, S., Tabelow, K., Voss, H. U., Anwander, A., Heidemann, R. M. & Polzehl, J. (2012), ‘Position-orientation adaptive smoothing of diffusion weighted magnetic resonance data (poas)’, *Medical image analysis* **16**(6), 1142–1155.
- Boyd, S., Parikh, N., Chu, E., Peleato, B., Eckstein, J. et al. (2011), ‘Distributed optimization and statistical learning via the alternating direction method of multipliers’, *Foundations and Trends® in Machine learning* **3**(1), 1–122.
- de Groot, M., Vernooij, M. W., Klein, S., Ikram, M. A., Vos, F. M., Smith, S. M., Niessen, W. J. & Andersson, J. L. (2013), ‘Improving alignment in tract-based spatial statistics: Evaluation and optimization of image registration’, *NeuroImage* **76**, 400 – 411.
- Descoteaux, M., Angelino, E., Fitzgibbons, S. & Deriche, R. (2007), ‘Regularized, fast, and robust analytical q-ball imaging’, *Magnetic resonance in medicine* **58**(3), 497–510.
- Descoteaux, M., Deriche, R., Knosche, T. R. & Anwander, A. (2009), ‘Deterministic and probabilistic tractography based on complex fibre orientation distributions’, *IEEE transactions on medical imaging* **28**(2), 269–286.
- Essen, D. C. V., Smith, S. M., Barch, D. M., Behrens, T. E., Yacoub, E. & Ugurbil, K.

- (2013), ‘The wu-minn human connectome project: An overview’, *NeuroImage* **80**, 62 – 79.
- Fan, J. & Gijbels, I. (1996), *Local polynomial modelling and its applications: monographs on statistics and applied probability 66*, Vol. 66, CRC Press.
- Glasser, M. F., Sotiropoulos, S. N., Wilson, J. A., Coalson, T. S., Fischl, B., Andersson, J. L., Xu, J., Jbabdi, S., Webster, M., Polimeni, J. R., Van Essen, D. C. & Jenkinson, M. (2013), ‘The minimal preprocessing pipelines for the human connectome project’, *NeuroImage* **80**, 105 – 124.
- Gudbjartsson, H. & Patz, S. (1995), ‘The rician distribution of noisy mri data’, *Magnetic resonance in medicine* **34**(6), 910–914.
- Hahn, K. R., Prigarin, S., Heim, S. & Hasan, K. (2006), Random noise in diffusion tensor imaging, its destructive impact and some corrections, *in* ‘Visualization and Processing of Tensor Fields’, Springer, pp. 107–119.
- Hua, K., Zhang, J., Wakana, S., Jiang, H., Li, X., Reich, D. S., Calabresi, P. A., Pekar, J. J., van Zijl, P. C. & Mori, S. (2008), ‘Tract probability maps in stereotaxic spaces: Analyses of white matter anatomy and tract-specific quantification’, *NeuroImage* **39**, 336 – 347.
- Jenkinson, M., Bannister, P., Brady, M. & Smith, S. (2002), ‘Improved optimization for the robust and accurate linear registration and motion correction of brain images’, *NeuroImage* **17**, 825 – 841.
- Jenkinson, M., Beckmann, C. F., Behrens, T. E., Woolrich, M. W. & Smith, S. M. (2012), ‘Fsl’, *NeuroImage* **62**, 782 – 790.
- Jensen, J. H., Glenn, G. R. & Helpert, J. A. (2016), ‘Fiber ball imaging’, *Neuroimage* **124**, 824–833.
- Le Bihan, D. & Warach, S. J. (1995), ‘Diffusion and perfusion magnetic resonance imaging: Applications to functional mri.’.

- Li, Y., Zhu, H., Shen, D., Lin, W., Gilmore, J. H. & Ibrahim, J. G. (2011), ‘Multiscale adaptive regression models for neuroimaging data’, *Journal of the Royal Statistical Society: Series B (Statistical Methodology)* **73**(4), 559–578.
- Liu, M., Vemuri, B. C. & Deriche, R. (2013), ‘A robust variational approach for simultaneous smoothing and estimation of dti’, *NeuroImage* **67**, 33–41.
- McCarthy, P. (2020), ‘Fsleyes 0.34.0; <https://doi.org/10.5281/zenodo.3937147>’.
- Mori, S. (2007), *Introduction to diffusion tensor imaging*, Elsevier.
- Muschelli, J. (2018), *neurohcp: Human ‘Connectome’ Project Interface*. R package version 0.8.1.  
**URL:** <https://db.humanconnectome.org>
- Muschelli, J., Sweeney, E., Lindquist, M. & Crainiceanu, C. (2015), ‘fslr: Connecting the fsl software with r’, *The R Journal* **7**(1), 163–175.
- Narcowich, F. J., Petrushev, P. & Ward, J. D. (2006a), ‘Localized tight frames on spheres’, *SIAM Journal on Mathematical Analysis* **38**(2), 574–594.
- Narcowich, F., Petrushev, P. & Ward, J. (2006b), ‘Decomposition of besov and triebel–lizorkin spaces on the sphere’, *Journal of Functional Analysis* **238**(2), 530–564.
- Polzehl, J. & Spokoiny, V. (2006), ‘Propagation-separation approach for local likelihood estimation’, *Probability Theory and Related Fields* **135**(3), 335–362.
- Polzehl, J. & Spokoiny, V. G. (2000), ‘Adaptive weights smoothing with applications to image restoration’, *Journal of the Royal Statistical Society: Series B (Statistical Methodology)* **62**(2), 335–354.
- Raj, A., Hess, C. & Mukherjee, P. (2011), ‘Spatial hardi: improved visualization of complex white matter architecture with bayesian spatial regularization’, *Neuroimage* **54**(1), 396–409.

- Rao, S., Ibrahim, J. G., Cheng, J., Yap, P.-T. & Zhu, H. (2016), ‘Sr-hardi: Spatially regularizing high angular resolution diffusion imaging’, *Journal of Computational and Graphical Statistics* **25**(4), 1195–1211.
- Sporns, O. (2010), *Networks of the Brain*, MIT press.
- Tabelow, K., Polzehl, J., Spokoiny, V. & Voss, H. U. (2008), ‘Diffusion tensor imaging: structural adaptive smoothing’, *NeuroImage* **39**(4), 1763–1773.
- Tournier, J.-D., Calamante, F. & Connelly, A. (2007), ‘Robust determination of the fibre orientation distribution in diffusion mri: non-negativity constrained super-resolved spherical deconvolution’, *Neuroimage* **35**(4), 1459–1472.
- Tournier, J.-D., Calamante, F., Gadian, D. G. & Connelly, A. (2004), ‘Direct estimation of the fiber orientation density function from diffusion-weighted mri data using spherical deconvolution’, *NeuroImage* **23**(3), 1176–1185.
- Tuch, D. S. (2004), ‘Q-ball imaging’, *Magnetic resonance in medicine* **52**(6), 1358–1372.
- Tuch, D. S., Reese, T. G., Wiegell, M. R., Makris, N., Belliveau, J. W. & Wedeen, V. J. (2002), ‘High angular resolution diffusion imaging reveals intravoxel white matter fiber heterogeneity’, *Magnetic resonance in medicine* **48**(4), 577–582.
- Van Essen, D. C., Smith, S. M., Barch, D. M., Behrens, T. E., Yacoub, E., Ugurbil, K., Consortium, W.-M. H. et al. (2013), ‘The wu-minn human connectome project: an overview’, *Neuroimage* **80**, 62–79.
- Wakana, S., Caprihan, A., Panzenboeck, M. M., Fallon, J. H., Perry, M., Gollub, R. L., Hua, K., Zhang, J., Jiang, H., Dubey, P., Blitz, A., van Zijl, P. & Mori, S. (2007), ‘Reproducibility of quantitative tractography methods applied to cerebral white matter’, *NeuroImage* **36**, 630 – 644.
- Wong, R. K., Lee, T. C., Paul, D. & Peng, J. (2016), ‘Fiber direction estimation, smoothing and tracking in diffusion mri’, *The annals of applied statistics* **10**(3), 1137.

- Woolrich, M. W., Jbabdi, S., Patenaude, B., Chappell, M., Makni, S., Behrens, T., Beckmann, C., Jenkinson, M. & Smith, S. M. (2009), ‘Bayesian analysis of neuroimaging data in fsl’, *NeuroImage* **45**, S173 – S186.
- Yan, H., Carmichael, O., Paul, D. & Peng, J. (2018), ‘Estimating fiber orientation distribution from diffusion mri with spherical needlets’, *Medical image analysis* **46**, 57–72.
- Yu, T. & Li, P. (2013), ‘Spatial shrinkage estimation of diffusion tensors on diffusion-weighted imaging data’, *Journal of the American Statistical Association* **108**(503), 864–875.
- Zhang, Y., Brady, M. & Smith, S. (2001), ‘Segmentation of brain mr images through a hidden markov random field model and the expectation-maximization algorithm’, *IEEE Transactions on Medical Imaging* **20**, 45–57.

# Supplementary Text

## S.1 Synthetic experiments: additional details

### S.1.1 2D ROI simulation I

Table S.1: **2D ROI simulation I**: Hellinger distance.

Estimator	True FODs		Noiseless estimates	
	Mean H-dist.	SD H-dist.	Mean H-dist.	SD H-dist.
SN-lasso(noiseless)	0.446	0.047	-	-
SN-lasso(voxel-wise)	0.498	0.053	0.225	0.128
NARM( $\alpha = 0.10$ )	0.470	0.038	0.179	0.075
NARM( $\alpha = 0.15$ )	0.470	0.038	0.182	0.076
NARM( $\alpha = 0.20$ )	0.470	0.038	0.180	0.076
NARM(no stopping&rescaling)	0.509	0.054	0.329	0.103
NARM(no stopping)	0.510	0.054	0.325	0.115
NARM(no rescaling)	0.470	0.039	0.181	0.077
NARM( $\chi^2$ -stopping, $c = 3$ )	0.471	0.043	0.203	0.086
NARM( $\chi^2$ -stopping, $c = 4$ )	0.473	0.043	0.210	0.094
PMARM( $c = 0.15$ )	0.476	0.043	0.220	0.103
PMARM( $c = 0.20$ )	0.477	0.048	0.225	0.110
PMARM( $c = 0.25$ )	0.478	0.048	0.230	0.112

## S.1.2 2D ROI simulation II

Table S.2: **2D ROI simulation II**: Hellinger distance.

Estimator	True FODs		Noiseless estimates	
	Mean H-dist.	SD H-dist.	Mean H-dist.	SD H-dist.
SN-lasso(noiseless)	0.357	0.194	-	-
SN-lasso(voxel-wise)	0.404	0.202	0.169	0.147
NARM( $\alpha = 0.10$ )	0.380	0.200	0.135	0.113
NARM( $\alpha = 0.15$ )	0.380	0.201	0.138	0.116
NARM( $\alpha = 0.20$ )	0.380	0.201	0.138	0.117
NARM(no stopping&rescaling)	0.542	0.078	0.418	0.154
NARM(no stopping)	0.449	0.201	0.320	0.187
NARM(no rescaling)	0.380	0.201	0.136	0.116
NARM( $\chi^2$ -stopping, $c = 2$ )	0.414	0.189	0.189	0.157
NARM( $\chi^2$ -stopping, $c = 3$ )	0.413	0.190	0.194	0.158
NARM( $\chi^2$ -stopping, $c = 4$ )	0.415	0.191	0.200	0.162
PMARM( $c = 0.05$ )	0.385	0.203	0.167	0.131
PMARM( $c = 0.10$ )	0.377	0.204	0.268	0.195



### S.1.3 3D ROI simulation at $b = 1000s/mm^2$

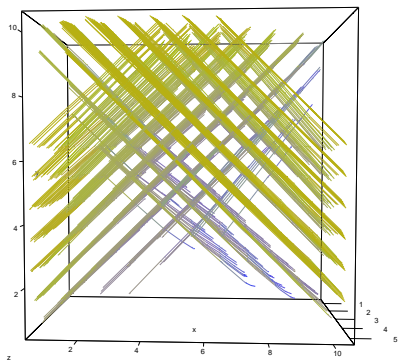
Table S.3: **3D ROI simulation**: Hellinger distance.

Estimator	True FODs		Noiseless estimates	
	Mean H-dist.	SD H-dist.	Mean H-dist.	SD H-dist.
SN-lasso(noiseless)	0.379	0.135	-	-
SN-lasso(voxel-wise)	0.450	0.165	0.234	0.171
NARM( $\alpha = 0.15$ )	0.402	0.143	0.144	0.099
NARM(no stopping&rescaling)	0.457	0.096	0.252	0.161
PMARM( $c = 0.05$ )	0.422	0.151	0.201	0.140
PMARM( $c = 0.10$ )	0.445	0.117	0.225	0.151

Figure S.1: **3D ROI simulation**: Tracking results. (a) True FODs in SH basis; (b) SN-lasso (voxel-wise) estimates; (c) NARM ( $\alpha = 0.15$ ) estimates; (d) NARM (no stopping&rescaling) estimates; (e) PMARM ( $c = 0.05$ ) estimates; (f) PMARM ( $c = 0.10$ ) estimates.

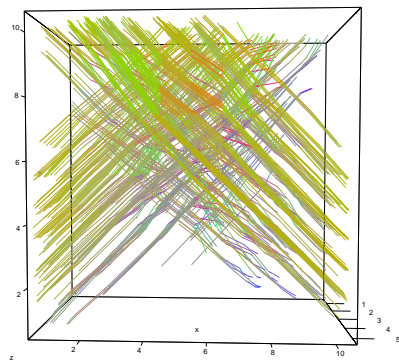
(a) True FODs

(fiber number: 451, fiber length: 5.59)



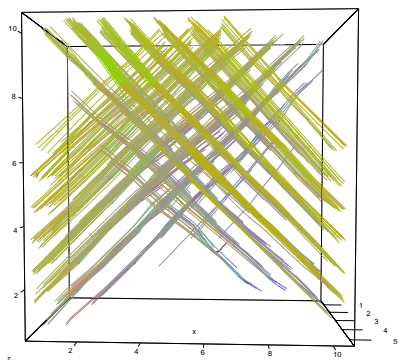
(b) SN-lasso (voxel-wise)

(fiber number: 392, fiber length: 4.11)



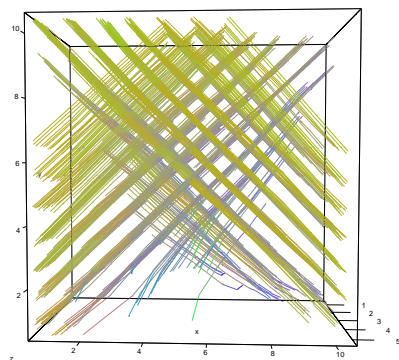
(c) NARM( $\alpha = 0.15$ )

(fiber number: 420, fiber length: 4.63)



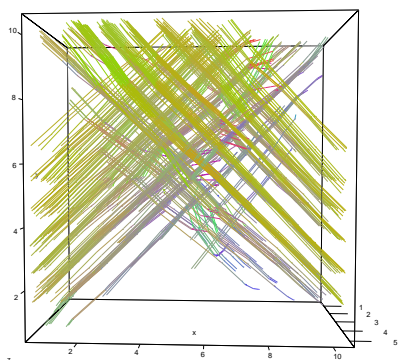
(d) NARM(no stopping&rescaling)

(fiber number: 489, fiber length: 5.43)



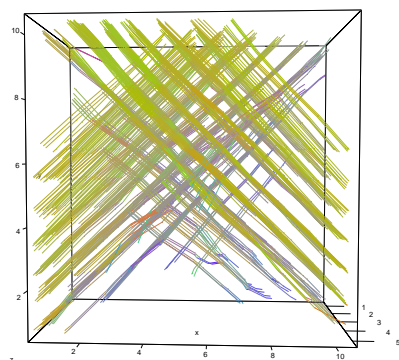
(e) PMARM( $c=0.05$ )

(fiber number: 398, fiber length: 4.23)



(f) PMARM( $c=0.10$ )

(fiber number: 440, fiber length: 4.75)





### S.1.4 3D ROI simulation at $b = 3000s/mm^2$

Figure S.2: **3D ROI simulation** ( $b = 3000s/mm^2$ ): FOD estimates on  $z$ -slice 2. (a) True FODs; (b) SN-lasso (voxel-wise) estimates; (c) NARM ( $\alpha = 0.15$ ) estimates; (d) NARM (no stopping&rescaling) estimates; (e) PMARM ( $c = 0.05$ ) estimates; (f) PMARM ( $c = 0.10$ ) estimates.

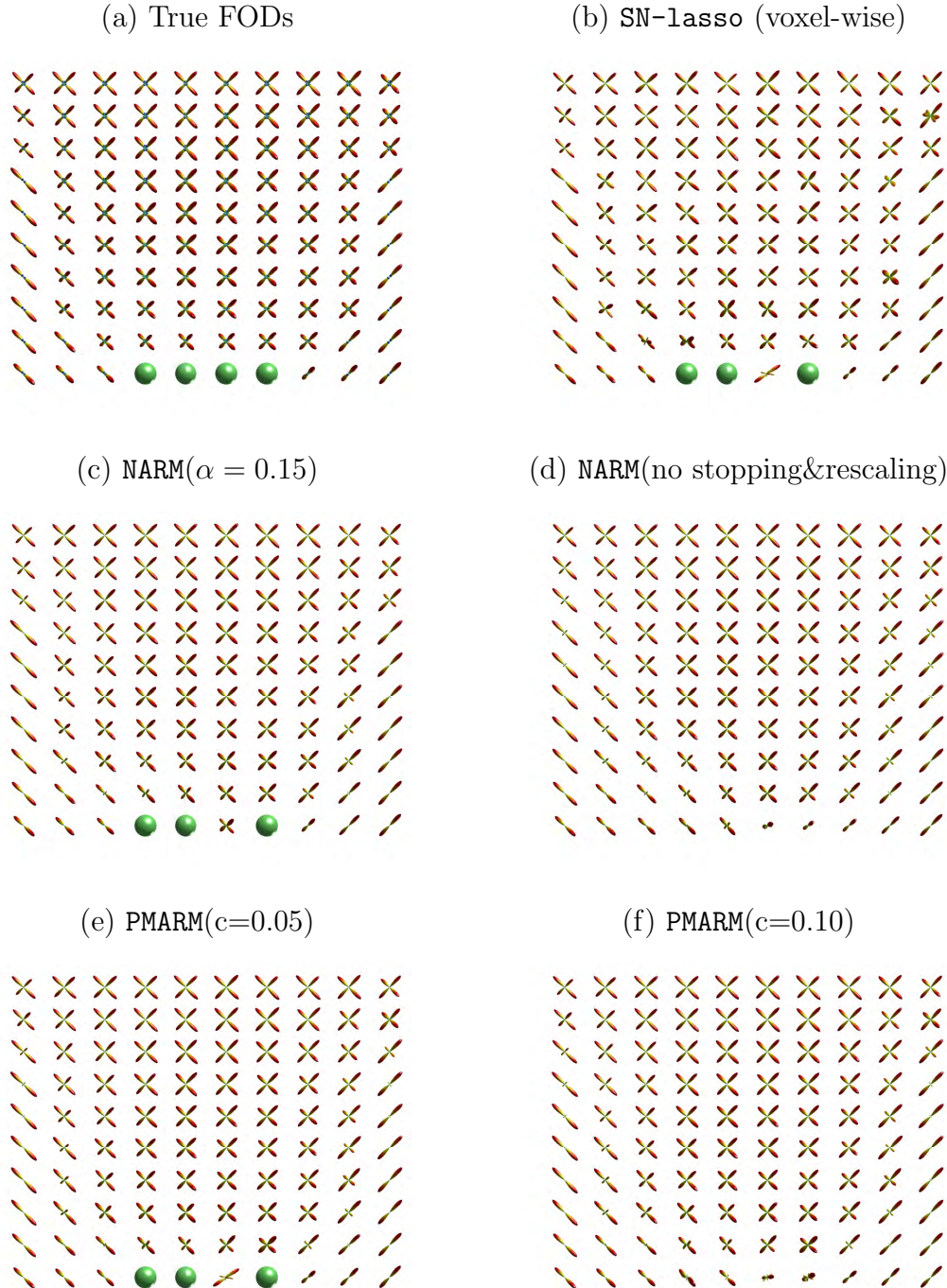
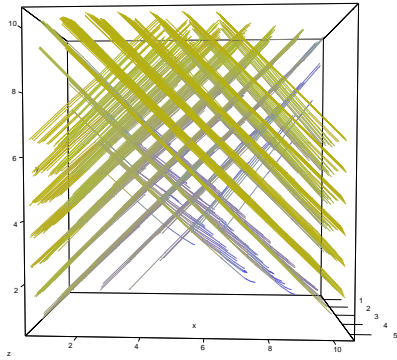


Figure S.3: **3D ROI simulation** ( $b = 3000s/mm^2$ ): Tracking results. (a) True FODs; (b) SN-lasso (voxel-wise) estimates; (c) NARM ( $\alpha = 0.15$ ) estimates; (d) NARM (no stopping&rescaling) estimates; (e) PMARM ( $c = 0.05$ ) estimates; (f) PMARM ( $c = 0.10$ ) estimates.

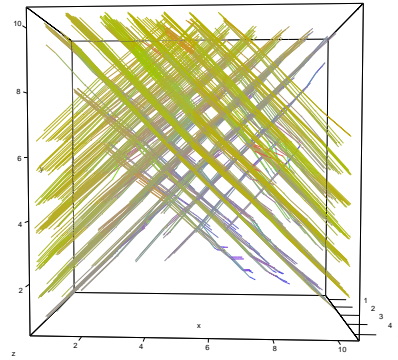
(a) True FODs

(fiber number: 451, fiber length: 5.59)



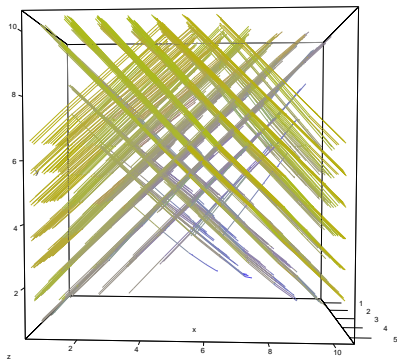
(b) SN-lasso (voxel-wise)

(fiber number: 430, fiber length: 4.68)



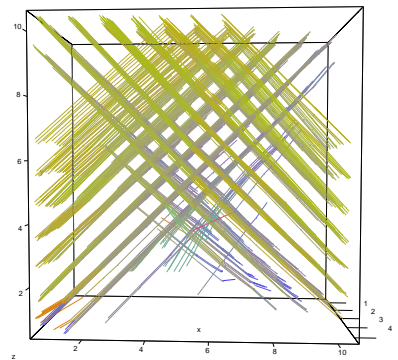
(c) NARM( $\alpha = 0.15$ )

(fiber number: 439, fiber length: 4.90)



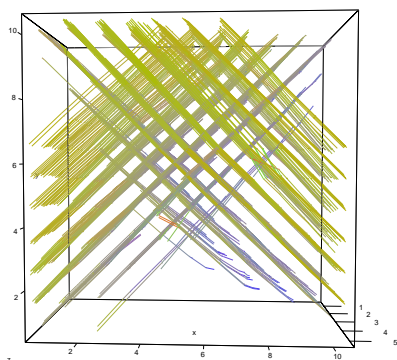
(d) NARM(no stopping&rescaling)

(fiber number: 490, fiber length: 5.64)



(e) PMARM( $c=0.05$ )

(fiber number: 444, fiber length: 4.99)



(f) PMARM( $c=0.10$ )

(fiber number: 488, fiber length: 5.65)

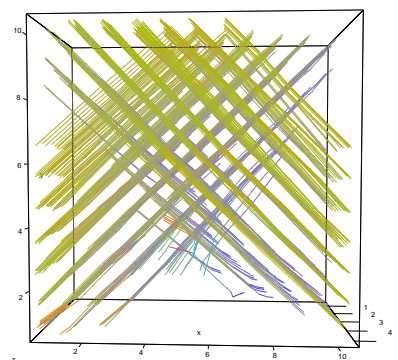


Table S.4: **3D ROI simulation** ( $b = 3000s/mm^2$ ): Success rate and angular error.

Estimator	0-Fiber	1-Fiber		2-Fiber	
	Co./Ov.	Co./Ov./Un.	Err.	Co./Ov./Un.	Err.
SN-lasso(noiseless)	1.00/0.00	1.00/0.00/0.00	1.60	1.00/0.00/0.00	1.68
SN-lasso(voxel-wise)	0.92/0.08	1.00/0.00/0.00	1.96	0.94/0.06/0.00	3.35
NARM( $\alpha = 0.15$ )	0.98/0.02	0.97/0.03/0.00	1.82	1.00/0.00/0.00	2.42
NARM(no stopping&rescaling)	0.27/0.73	0.79/0.21/0.00	2.62	1.00/0.00/0.00	2.29
PMARM( $c = 0.05$ )	0.88/0.12	0.93/0.07/0.00	1.95	0.99/0.01/0.00	2.22
PMARM( $c = 0.10$ )	0.31/0.69	0.85/0.15/0.00	2.13	1.00/0.00/0.00	2.28

Table S.5: **3D ROI simulation** ( $b = 3000s/mm^2$ ): Hellinger distance.

Estimator	True FODs		Noiseless estimates	
	Mean H-dist.	SD H-dist.	Mean H-dist.	SD H-dist.
SN-lasso(noiseless)	0.373	0.134	-	-
SN-lasso(voxel-wise)	0.398	0.137	0.160	0.102
NARM( $\alpha = 0.15$ )	0.382	0.135	0.114	0.077
NARM(no stopping&rescaling)	0.438	0.111	0.208	0.167
PMARM( $c = 0.05$ )	0.387	0.131	0.139	0.101
PMARM( $c = 0.10$ )	0.429	0.109	0.191	0.157

## S.2 Real D-MRI data experiments: additional details

### S.2.1 Single tensor model

The single tensor model (Le Bihan & Warach 1995, Basser & Jones 2002, Mori 2007) for the diffusion weighted signal  $S(\mathbf{u})$  along the gradient direction  $\mathbf{u}$  is

$$S(\mathbf{u}) = S_0 \exp(-b\mathbf{u}^T \mathbf{D} \mathbf{u}),$$

where  $\mathbf{D}$  is a  $3 \times 3$  positive definite matrix, known as the diffusion tensor. Let  $\lambda_1$ ,  $\lambda_2$  and  $\lambda_3$  be three eigenvalues of  $\mathbf{D}$ , the fractional anisotropy (FA) and the mean diffusivity (MD)

are then defined as:

$$\text{FA} = \frac{\sqrt{(\lambda_1 - \lambda_2)^2 + (\lambda_2 - \lambda_3)^2 + (\lambda_3 - \lambda_1)^2}}{\sqrt{2(\lambda_1^2 + \lambda_2^2 + \lambda_3^2)}}, \quad \text{MD} = \frac{\lambda_1 + \lambda_2 + \lambda_3}{3}.$$

$\text{FA} \in [0, 1]$  can be regarded as the indicator of diffusion pattern, where large FA indicates anisotropic diffusion along the principle eigenvector of  $\mathbf{D}$ , and small FA indicates isotropic diffusion (if the single tensor model holds). On the other hand, MD describes the diffusion rate, where large MD indicates fast diffusion and small MD indicates slow diffusion.